

# Probing Scaffold Size Effects on Multivalent Lectin-Glycan Binding Affinity, Thermodynamics and Antiviral Potency Using Polyvalent Glycan-Gold Nanoparticles

Rahman Basaran,<sup>1</sup> Darshita Budhadev,<sup>1</sup> Amy Kempf,<sup>2</sup> Inga Nehlmeier,<sup>2</sup> Nicole Hondow,<sup>4</sup> Stefan Pöhlmann,<sup>2,3</sup> Yuan Guo,<sup>5,\*</sup> and Dejian Zhou<sup>1,\*</sup>

<sup>1</sup> School of Chemistry and Astbury Centre for Structural Molecular Biology, University of Leeds, Leeds LS2 9JT, United Kingdom. Email: [d.zhou@leeds.ac.uk](mailto:d.zhou@leeds.ac.uk).

<sup>2</sup> Infection Biology Unit, German Primate Center - Leibniz Institute for Primate Research, 37077 Göttingen, Germany.

<sup>3</sup> Faculty of Biology and Psychology, Georg-August-University Göttingen, 37073 Göttingen, Germany.

<sup>4</sup> School of Chemical and Process Engineering, University of Leeds, Leeds LS2 9JT, United Kingdom.

<sup>5</sup> School of Food Science and Nutrition, and Astbury Centre for Structural Molecular Biology, University of Leeds, Leeds LS2 9JT, United Kingdom. Email: [y.guo@leeds.ac.uk](mailto:y.guo@leeds.ac.uk).

**Keywords:** multivalent lectin-glycan interaction, glycoconjugate, gold nanoparticle, biophysical probe, viral inhibition

## Abstract

Multivalent lectin-glycan interactions (MLGIs) are pivotal for viral infections and immune regulation. Their structural and biophysical data are thus highly valuable, not only for the understanding of basic mechanisms but also for designing potent glycoconjugate therapeutics against target MLGIs. However, such information for some important MGLIs remain poorly understood, which has greatly limited the research progress in this area. We have recently developed densely glycosylated nanoparticles (*e.g.*, ~4 nm quantum dot (QD) or ~5 nm gold nanoparticle (GNP)) as new mechanistic probes for MLGIs. Using two important tetrameric viral receptors, DC-SIGN and DC-SIGNR as model lectins, we have shown these probes not only can offer sensitive fluorescence readouts for MLGI affinity quantification, but also reveal key structural information (*e.g.*, binding site orientation and binding mode) that are very useful for MLGI targeting. However, the relatively small sizes of scaffolds may not be optimal for maximizing MLGI affinity and targeting specificity. Herein, using  $\alpha$ -manno- $\alpha$ -1,2-biose (DiMan) functionalized GNPs (GNP-DiMan) probes, we have systematically studied how GNP scaffold size (*e.g.*, 5, 13, and 27 nm) and glycan density (*e.g.*, 100, 75, 50 and 25%) determine their MLGI affinities, thermodynamics, and antiviral properties. We have developed a new GNP fluorescence quenching assay format for quantifying MLGI affinity to minimize the potential interference from GNP's strong

inner filter effect, revealing that increasing GNP size is highly beneficial to enhance MLGI affinity. We have further determined the MLGI thermodynamics by combining temperature-dependent affinity measurement and Van't Hoff analysis, revealing that GNP-DiMan-DC-SIGN/R binding is enthalpy driven. Finally, we find that increasing GNP size significantly enhances the antiviral potency. Notably, the DiMan functionalised 27 nm GNP (G27-DiMan) potently and robustly blocks both DC-SIGN and DC-SIGNR mediated pseudo-Ebola virus cellular entry with an  $EC_{50}$  of  $\sim 23$  and  $\sim 49$  pM, respectively, placing it the most potent glycoconjugate entry inhibitor against DC-SIGN/R mediated Ebola cellular infections.

## Introduction

Multivalent lectin-glycan interactions (MLGIs) are widespread and vital for pathogen infection and immune regulation.<sup>1-5</sup> As monovalent lectin-glycan interactions are often too weak to be bio-active, lectins mostly form multimeric structures with clustered carbohydrate-binding-domains (CRDs), allowing them to bind multivalently with multivalent glycan ligands to enhance affinity and define specificity *via* spatial matching. The overall MLGI affinity is not only defined by the monovalent affinity, but also the binding mode and glycan valency.<sup>3</sup> In general, a pair of spatially matched MLGI partners may bind simultaneously with each other to form small individual lectin-ligand complexes, giving rise to a great MLGI affinity enhancement due to both favourable binding enthalpy and entropy terms.<sup>6-8</sup> While those without the perfect spatial- and orientational- matches may crosslink each other to maximize the binding enthalpies, but this often forms large-scale protein-ligand assemblies with relatively low MLGI affinity enhancement due to large entropic penalties.<sup>9</sup> Therefore, understanding the structural and molecular mechanisms of target MLGIs is of great importance, allowing us to design spatial-matched glycoconjugates to target specific MLGIs potently for therapeutical interventions. Notably, the development of glycoconjugates as potent entry inhibitors to block virus binding and infecting host cells can be advantageous over other anti-viral strategies because this can effectively prevent virus mutation and develop resistance.<sup>4, 10-11</sup> This can be particularly beneficial for controlling infections induced by unstable RNA viruses, including SARS-CoV-2, where rapid mutations and variations can lead to effective evasion of host antibody responses induced by past infections and/or vaccines.

A large number of glycoconjugates, built upon various scaffolds, have been widely employed as probes to study MLGI properties and also exploited as potential therapeutics.<sup>3-5, 7, 11-21</sup> Some of these have exhibited potent anti-pathogenic infection properties.<sup>6-7, 11, 15-16, 18-20</sup> In most cases, their MLGI

biophysical data were measured by conventional techniques, such as surface plasmon resonance (SPR),<sup>4, 22</sup> isothermal titration calorimetry (ITC),<sup>4, 23</sup> and/or fluorescence competition assays.<sup>24-25</sup> While ITC and SPR are widely used biophysical techniques which can provide quantitative binding affinity, thermodynamics, and/or kinetics data, they cannot provide key structural information, such as lectin binding site orientation, inter-binding site distance, and binding mode, which are very useful for designing potent, specific glycoconjugate inhibitors. Moreover, these methods can also suffer from limitations, such as low sensitivity (requiring large sample amounts), and unreliable binding affinity measurement for very strong interactions (with equilibrium dissociation constants,  $K_{ds}$ , of low nM or below) for ITC,<sup>23, 26</sup> while the affinities measured by SPR can be strongly affected by the density and orientation of the immobilised binding partners.<sup>22</sup> Furthermore, most previous MLGI studies have been based on the “passive” scaffolds, where nanomaterials are used as scaffolds only to create a polyvalent display of glycans to enhance their MLGI affinity, specificity, and/or therapeutic potency. The unique size-dependent optical/electrical properties of nano-scaffolds, the cornerstones of many nanomaterials, have not been explored as readouts for probing MLGI biophysical and structural data.

Recently, we have developed the “active” nano-scaffold strategy for MLGI research, where we have not only exploited the nano-scaffolds’ unique optical properties as new MLGI affinity assays but also their nanoscale size and high TEM contrast to reveal key MLGI structural information.<sup>11, 19, 27-29</sup> We have employed the dendritic cell tetrameric lectin, DC-SIGN,<sup>30-31</sup> and a closely-related endothelial cell lectin, DC-SIGNR,<sup>32</sup> (collectively abbreviated as DC-SIGN/R here after) as model lectins. These lectins play a key role in mediating or facilitating the infection of many viruses, *e.g.*, HIV, HCV, Ebola, Zika, and SARS-CoV-2.<sup>20-21, 30, 32-33</sup> Despite displaying identical CRD-mannose monovalent binding motifs,<sup>34</sup> and almost identical tetrameric architectures,<sup>31, 35</sup> DC-SIGN/R in fact exhibit distinct virus transmitting properties. For example, DC-SIGN is more effective than DC-SIGNR in transmitting the HIV infection,<sup>36</sup> while only DC-SIGNR, but not DC-SIGN, is able to transmit the West Nile virus infection.<sup>37</sup> The structural mechanisms underlying such differences in DC-SIGN/R remain not fully understood. By displaying glycans polyvalently onto a CdSe/ZnS quantum dot (QD)<sup>19, 27-28</sup> or a small gold nanoparticle (GNP) scaffold<sup>11</sup> as multifunctional probes, we have developed a new ratiometric QD-FRET (Förster resonance energy transfer)<sup>19, 27-28</sup> or GNP-fluorescence quenching affinity assay for MLGIs.<sup>11</sup> We have found that glycan-nanoparticles exhibit greatly enhanced MLGI affinities than the corresponding monovalent binding (up to 1.8 million folds)<sup>29</sup> and the enhancement with DC-SIGN is significantly greater than that with DC-SIGNR (by ~20-200 folds), arising from their distinct binding modes: DC-SIGN binds tetravalently with all 4 CRDs to one glycan-nanoparticle, while DC-SIGNR crosslinks with multiple glycan-nanoparticles.<sup>11, 19, 28</sup> These glycan-nanoparticles was found to potently

block DC-SIGN-, but not DC-SIGNR-, mediated pseudo-Ebola virus infections with sub-nM levels of  $EC_{50}$  values ( $EC_{50}$ : the concentration giving 50% inhibition).<sup>11, 19</sup> Despite success, our previous studies are built upon small nanoparticle scaffolds (e.g., ~4 nm QD or 5 nm GNP), which may not be optimal for maximising the MLGI affinity, specificity, and antiviral potency.

In this paper, we have systematically varied the GNP scaffold size (e.g., ~5, ~13 and ~27 nm) and their surface glycan densities (e.g., 100, 75, 50 and 25%, by diluting the active glycan ligand, lipoic acid-tetra(ethylene glycol)- $\alpha$ -manno- $\alpha$ -1,2-biose (LA-EG<sub>4</sub>-DiMan) using an inert spacer ligand, LA-EG<sub>4</sub>-OH) to investigate how these factors control their MLGI properties with DC-SIGN/R (**Fig. 1**). Moreover, we have developed a new format of GNP-fluorescence quenching assay to minimize the interference arising from GNP's strong inner filter effect, allowing us to robustly quantify MLGI affinities for both small and large GNP-glycans. We find that the MLGI affinities between DC-SIGN/R and GNP-glycans are enhanced significantly with the increasing GNP size, while reducing glycan density from 100% to 50% does not markedly affect their affinity, although reducing the glycan density further to 25% weakens their affinity. By quantifying temperature-dependent MLGI affinities *via* GNP fluorescence quenching and applying Van't Hoff analysis, we have quantified their MLGI biophysical parameters, revealing that DC-SIGN/R bindings with GNP-glycans are enthalpy driven, and the negative binding enthalpy changes ( $\Delta H$ s) for DC-SIGN are ~4 times that of the monovalent binding, while that for DC-SIGNR is about twice that of the monovalent binding, under our assay conditions. Finally, we report that the glycan-GNPs potently block DC-SIGN/R mediated pseudo-Ebola viral infection of host cells, with potencies being enhanced with the increasing GNP size. In particular, a 27 nm GNP capped with the pure LA-EG<sub>4</sub>-DiMan ligand (G27-DiMan) potently and robustly blocks both DC-SIGN and DC-SIGNR mediated virus infections with an  $EC_{50}$  value of ~23 and ~49 pM, respectively, making it the most potent glycoconjugate inhibitor against DC-SIGN/R mediated Ebola cellular infection. Together, our results have revealed the critical important role of GNP scaffold size in controlling their MLGI biophysical parameters and blocking DC-SIGN/R-mediated virus entry.

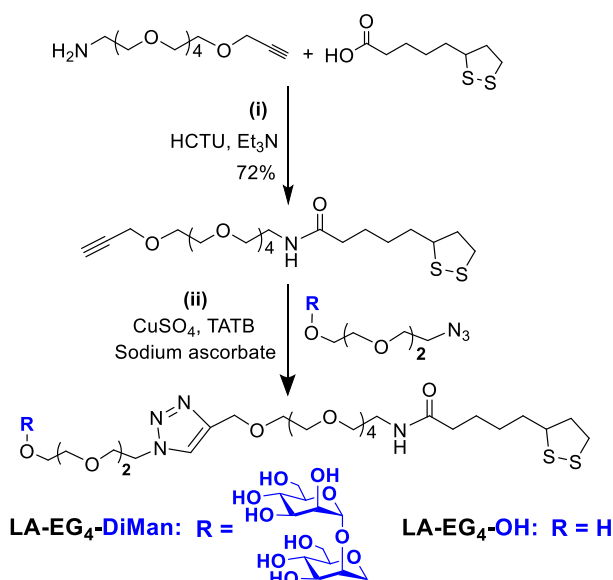
## Results and Discussion

**Ligand Design and Synthesis.** A lipoic acid-tetra(ethylene glycol)- $\alpha$ -manno- $\alpha$ -1,2-biose (LA-EG<sub>4</sub>-DiMan) based multifunctional ligand was synthesised *via* our established procedures (see Fig. 1 for its chemical structure).<sup>11</sup> Each ligand was designed to contain three unique functional domains:<sup>19, 38</sup> a LA anchoring domain to chelate strongly on the GNP surface by forming two strong Au-S bonds;<sup>11, 38</sup> a hydrophilic flexible EG<sub>4</sub> linker domain to offer high water solubility, excellent biocompatibility and

resistance against non-specific interactions;<sup>39-42</sup> and a terminal DiMan domain to promote strong and specific binding with DC-SIGN/R.<sup>14, 19</sup> A hydroxyl group (OH) terminating ligand having the same anchoring and EG<sub>4</sub> linker domains, LA-EG<sub>4</sub>-OH, (see Fig. 1 for its chemical structure) was also synthesized and employed as a spacer ligand to tune the GNP surface glycan density. It also served as a negative control to correct the fluorescence quenching background (in the absence of specific MLGIs) caused by GNP's inner filter effect. We showed previously that displaying LA-EG<sub>n</sub>-DiMan based glycan ligands polyvalently onto QDs (n = 3, 11)<sup>19, 28</sup> or G5 (n = 2)<sup>11</sup> yielded strong MLGI affinities with DC-SIGN,<sup>11, 19</sup> while those coated with the equivalent OH terminating ligands (with no terminal DiMan group) gave no measurable binding,<sup>28</sup> suggesting that LA-EG<sub>4</sub>-OH is a suitable negative control ligand here.

The synthetic route to the LA-EG<sub>4</sub>-DiMan and LA-EG<sub>4</sub>-OH spacer ligands was shown in Scheme 1. First, a LA-EG<sub>4</sub>-acetylene linker was synthesised by using the standard dicyclohexyl-carbodiimide /N,N-dimethyl aminopyridine (DCC/DMAP) mediated amide coupling between lipoic acid and H<sub>2</sub>N-EG<sub>4</sub>-acetylene.<sup>11</sup> Then,  $\alpha$ -1-manno- $\alpha$ -1,2-biose appending an EG<sub>2</sub>-azide linker (N<sub>3</sub>-EG<sub>2</sub>-DiMan, to offer some flexibility to the terminal DiMan group) was synthesised using our established route as described previously.<sup>19</sup> Finally, the LA-EG<sub>4</sub>-acetylene linker was efficiently coupled to N<sub>3</sub>-EG<sub>2</sub>-DiMan or N<sub>3</sub>-EG<sub>2</sub>-OH (commercial) *via* the Cu-catalyzed click chemistry to give the desired LA-EG<sub>4</sub>-DiMan or LA-EG<sub>4</sub>-OH ligand in good yields, respectively.<sup>11, 43</sup> Their chemical structures were confirmed by <sup>1</sup>H/<sup>13</sup>C NMR and LC-MS spectra (see SI for the details).

### Scheme 1. The Synthetic Route to the LA-EG<sub>4</sub>-DiMan and LA-EG<sub>4</sub>-OH spacer ligands.



**GNP Synthesis and Characterisation.** Three different-sized GNPs with an average diameter of  $\sim 5$ ,  $\sim 13$  and  $\sim 27$  nm (see SI, Figs. S1 and S2 for their TEM images), denoted as G5, G13 and G27, respectively, were employed in this study. Our motivation here was that tuning the GNP scaffold size may lead to an optimal glycan-GNP with excellent spatial and topological match to DC-SIGN/R, thereby greatly enhancing their MLGI affinity and selectivity with the target lectins.<sup>5</sup> The GNPs were either purchased commercially (for G5)<sup>11</sup> or synthesized in house (for G13 and G27) *via* the literature protocols with minor modifications as described in the experimental section.<sup>44-45</sup> Interestingly, the LA-EG<sub>4</sub>-DiMan ligand coated G5 particle (denoted as G5-DiMan) has a similar size and mannose coating to a gp160 trimer, the HIV surface densely glycosylated spike protein, which is responsible for mediating HIV-DC-SIGN interaction and viral infection.<sup>46-47</sup> Thus, G5-DiMan may serve as a good mimic of gp160 for probing its interaction with DC-SIGN. The larger G13 and G27 were employed to investigate how GNP scaffold size impacts their MLGIs with DC-SIGN/R. The citrate stabilized G13 and G27 as prepared gave a single plasmonic absorption band at  $\sim 520$  nm and  $\sim 522$  nm, respectively, and displayed a single distribution species with a hydrodynamic diameter ( $D_h$ , volume population) of  $\sim 16$  and  $\sim 29$  nm for G13 and G27, respectively, consistent to that expected for isolated single G13 and G27 particles coated with a thin layer of citrate ligands (SI, Figs. S1 and S2).

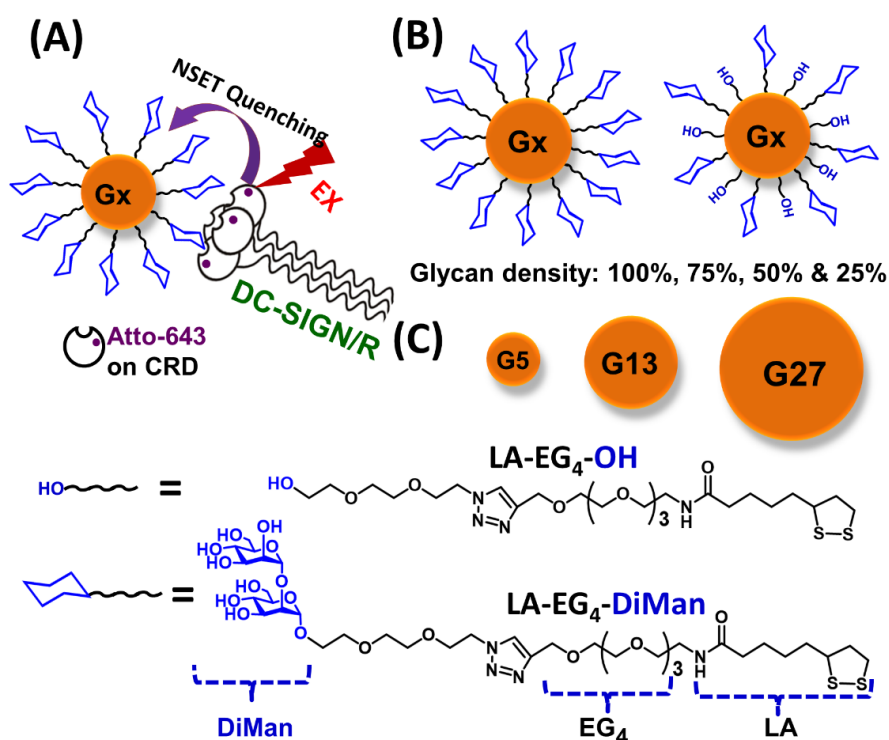


**Figure 1.** (A) Schematic showing the NSET quenching of DC-SIGN/R (labeled with Atto-643) fluorescence upon binding to a GNP-glycan. (B) Schematic representation of GNPs covered with 100% LA-based glycan ligands and LA-based glycan ligands with diluted to a surface glycan density of 75%, 50% and 25% using LA-

EG<sub>4</sub>-OH ligands. (C) Schematic showing the different sizes of GNPs (G<sub>x</sub>; x= 5, 13, and 27 nm) used in this study. (D) The chemical structures of LA-EG<sub>4</sub>-DiMan and LA-EG<sub>4</sub>-OH ligands.

**Preparation of GNP-glycan conjugates.** G<sub>x</sub>-glycan conjugates (G<sub>x</sub> capped with the corresponding LA-EG<sub>4</sub>-DiMan and/or LA-EG<sub>4</sub>-OH ligands) were prepared by incubation of citrate-stabilized GNPs overnight with the pure LA-EG<sub>4</sub>-DiMan or mixed LA-EG<sub>4</sub>-DiMan/LA-EG<sub>4</sub>-OH ligands (glycan ligand content varied from 100%, 75%, 50%, 25% to 0% to tune the GNP surface glycan ligand density) in water under a fixed total ligand: GNP molar ratio of 1000:1 for G5, 3000 for G13, or 10000 for G27. We have found previously that GNP-glycans prepared using the LA-glycan ligands and their reduced DHLA-forms have identical  $D_h$  value and stability.<sup>11</sup> Therefore, the air-stable LA-glycan ligands were directly used to make the GNP-glycans without reduction. Since the LA-EG<sub>4</sub>-DiMan and LA-EG<sub>4</sub>-OH spacer ligands have the same GNP anchoring and EG<sub>4</sub>-linker groups, they should have the same GNP binding properties. Therefore, the GNP surface ligand contents should be the same as those used in GNP conjugation and can be readily tuned by varying the solution glycan and spacer ligands ratio. The resulting G5-glycan conjugates were purified by ultra-filtration using 30K MWCO filter tubes and washing with pure water as described previously.<sup>11</sup> The G13- and G27- glycan conjugates were purified by centrifugation and washing with pure water. The unbound free ligands in the supernatant and washing were collected and used to determine the G<sub>x</sub> surface glycan valency.<sup>11</sup> The G<sub>x</sub>-glycan conjugates were found to completely resist NaCl (250 mM) induced aggregation, suggesting their surfaces were successfully functionalized with the desired ligands (the citrate stabilized GNPs readily aggregate in moderate NaCl content, due to effective screening their electrostatic repulsion). The G<sub>x</sub>-glycans were uniform and monodisperse in both water and a binding buffer (20 mM HEPES, 100 mM NaCl, 10 mM CaCl<sub>2</sub>, pH 7.8) with  $D_h$ s of ~13, ~22, and ~32 nm for G5-, G13- and G27- DiMan, respectively (SI, Figs. S5-S7). These  $D_h$ s were a few nm larger than their corresponding citrate stabilized G<sub>x</sub>s, as expected. The G<sub>x</sub>-glycan solutions were highly stable; no changes of physical appearance or precipitation were observed after prolonged storage (>12 months) in a fridge at 4 °C. The numbers of glycan ligands on each GNP (*i.e.*, glycan valency) were estimated from the ligand amount difference between that added and that remained unbound in the supernatant after GNP conjugation *via* a phenol-sulphuric acid carbohydrate quantification method as described previously<sup>11, 19, 48</sup> (see SI, Table S1). The average inter-glycan distance ( $d$ ) was estimated from their  $D_h$  value and glycan valency using the method reported previously,<sup>11, 49</sup> giving  $d$  values of ~0.95, ~0.93 and ~0.80 nm for G5-, G13- and G27- DiMan100%, respectively (SI, Table S2). These  $d$  values match well to the majority of inter-glycan sequon spaces (*e.g.* 0.7–1.3 nm) found on the HIV surface glycoprotein

gp160 trimer.<sup>46</sup> Therefore, our Gx-glycans are good mimics for probing the gp160-DC-SIGN interactions which are responsible for mediating the HIV infections.

**Quantifying GNP-glycan-DC-SIGN/R binding affinity.** GNPs are well-known for their strong and universal quenching property for a range of different fluorophores.<sup>50</sup> Moreover, its quenching efficiency (QE) - distance dependence has been shown to follow the nano-surface energy transfer (NSET, where QE is proportional to the inverse 4<sup>th</sup> power dependence on distance),<sup>51-53</sup> rather than the Förster resonance energy transfer (FRET, where QE is proportional to the inverse 6<sup>th</sup> power dependence on distance) mechanism experienced by organic quenchers. As a result, its quenching is far more efficient and able to cover a longer distance range than those relying on the FRET mechanism.<sup>50-51</sup> Indeed, the GNP's superior quenching ability has been widely exploited for biosensing, bioimaging and biodiagnostic applications.<sup>54-55</sup> Recently, we have demonstrated that GNP's outstanding fluorescence quenching can be harnessed as a new readout method for quantifying MLGI affinities using a small G5-glycan (**Fig. 1A**).<sup>11</sup> In that case, we first introduced a site-specific cysteine mutation on the CRD of the DC-SIGN/R extracellular segment. The mutation site lies at close to, but outside of, its glycan binding pocket, and therefore does not affect its glycan binding property. The mutant proteins have been shown to retain faithfully the tetrameric structure and glycan-binding properties of full-length lectins.<sup>11, 19, 27</sup> We then labeled the lectins using a maleimide-modified Atto-643 dye with a labeling efficiency of > 80% per monomer (SI, Fig. S11). Then, we measured the fluorescence spectra of the labeled lectins alone and their 1:1 molar mixtures with G5-glycans over a range of concentrations and fitted the obtained fluorescence quenching efficiency (QE) -concentration relationships using the Hill's equation to derive their apparent  $K_{ds}$ .<sup>11</sup> While this method worked well with the small G5-glycans, due to its relatively low absorption extinction coefficient ( $\epsilon = 1.10 \times 10^7 \text{ M}^{-1}\text{cm}^{-1}$ ), unfortunately, it cannot work for the larger GNP-glycans. This is because the GNP's  $\epsilon$  roughly increases linearly with volume,<sup>11, 56</sup> where the very strong absorption (hence inner filter effect) of the large GNPs (e.g.,  $\epsilon = 1.10 \times 10^7$ ,  $2.32 \times 10^8$  and  $2.39 \times 10^9 \text{ M}^{-1}\text{cm}^{-1}$  for G5, G13, and G27, respectively) can severely interfere with the fluorescence quenching measurement, especially at high concentrations (e.g. >10 nM).

To overcome this problem, a fixed concentration of 10, 4, or 0.5 nM for G5, G13, or G27, respectively, was employed while the lectin concentration was varied in this study. In this case, all lectin-Gx-DiMan binding samples had the same background absorption, which can be easily corrected by using the respective Gx-OH (Gx coated with purely LA-EG<sub>4</sub>-OH ligand) negative control at that concentration. The fluorescence spectra of the lectins (varying concentrations) without and with a fixed concentration of Gx-glycans were recorded under an excitation wavelength,  $\lambda_{ex}$ , of 630 nm, where Gxs have minimal

absorption, to reduce any possible interference. All binding studies were carried out in a binding buffer containing 1 mg/mL of bovine serum albumin (BSA) as described earlier,<sup>11</sup> to make the binding conditions more closely resemble real biological situations. Moreover, this also greatly reduced any non-specific interactions and adsorption of proteins and GNPs to surfaces, which can be a major source of experiments errors at low concentrations, *e.g.* < 10 nM.<sup>57</sup>

The fluorescence spectra showing the binding between DC-SIGN/R and Gx-DiMan were given in SI, Figs. S12-S17. In the absence of Gx-DiMan, DC-SIGN/R's fluorescence increased linearly with concentration, but their fluorescence was greatly reduced in the presence of Gx-DiMan, consistent with binding-induced fluorescence quenching by the GNPs in proximity.<sup>11, 50-51, 55</sup> Moreover, free mannose effectively competed with Gx-DiMan binding with DC-SIGN/R, giving rise to a significant, dose-dependent recovery of DC-SIGN/R fluorescence (SI, Figs. S19-20). Further, mixing DC-SIGN/R with the control Gx-OH produced negligible quenching, confirming that the fluorescence quenching observed with Gx-DiMan was due to specific MLGIs between Gx-DiMan and DC-SIGN/R (SI, Fig. S21).

To analyse the binding data quantitatively, we first calculated the quenching efficiency (QE) for each (Gx-DiMan + lectin) sample at each protein concentration *via* Eq. 1:<sup>11</sup>

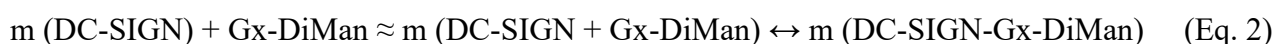
$$QE = (IF_0 - IF)/IF_0 \quad (\text{Eq. 1})$$

Where  $IF_0$  and  $IF$  are the integrated protein fluorescence signals in the absence and presence of Gx-DiMan, respectively.

Given that a GNP has been shown to quench fluorophores in close proximity by up to 99.97%,<sup>50</sup> it is safe to assume that the observed QE represents the fraction of the added lectins that have bound to Gx-DiMan.<sup>11</sup> Previously, we measured the QEs for 1:1 mixed lectin + G5-glycan samples at varied concentrations, and then fitted the QE - concentration relationships by the Hill equation to derive their apparent  $K_{ds}$ .<sup>11</sup> While this worked well for the small G5-glycans (due to relatively low its  $\epsilon$ ), it did not work for the large G13- and G27- glycans, owing to their much stronger inner filter effect (*e.g.*,  $\epsilon$  for G13 and G27 being  $\sim 21$  and  $\sim 220$  fold that of G5, respectively).<sup>11</sup>

Interestingly, we found that the QE stayed almost constant for a fixed amount of Gx-DiMan after mixing with DC-SIGN over a certain lectin: Gx molar ratio, although the QE was found to decrease as the lectin: Gx molar ratio was further increased, possibly due to surface saturation (see SI, Fig. S12).

This result suggests that, before surface saturation, Gx-DiMan surface-bound DC-SIGN molecules do not hinder further binding of other DC-SIGN molecules on the same Gx-DiMan; and Gx-DiMan with a few bound DC-SIGN molecules can still produce the same level of QE as free Gx-DiMan. Therefore, the equilibrium for multiple DC-SIGN molecules binding to one Gx-DiMan can be approximated as multiple copies of one-to-one DC-SIGN-Gx-DiMan binding interactions as Eq. 2 below.



Note here that each Gx-DiMan has been cycled  $m$  times in binding to  $m$  DC-SIGN molecules ( $m <$  lectin saturation number on each Gx-DiMan). As a result, the calculation of  $K_d$  can be greatly simplified by using the 1:1 binding equilibrium:



$$K_d = [\text{DC-SIGN}] [\text{Gx-DiMan}] / [\text{DC-SIGN-Gx-DiMan}] \quad (\text{Eq. 4})$$

Where  $[\text{DC-SIGN}]$ ,  $[\text{Gx-DiMan}]$ , and  $[\text{DC-SIGN-Gx-DiMan}]$  are equilibrium concentrations for free DC-SIGN, free Gx-DiMan, and bound DC-SIGN-Gx-DiMan complex, respectively.

For a 1:1 interaction with equal starting concentration for both components, where  $[\text{DC-SIGN}]_0 = [\text{Gx-DiMan}]_0 = C_0$ . Since the QE represents the portion of lectin bound to Gx-DiMan, thus  $[\text{DC-SIGN-Gx-DiMan}] = C_0 \times \text{QE}$ , thus the equilibrium free  $[\text{DC-SIGN}] = [\text{Gx-DiMan}] = C_0 \times (1 - \text{QE})$ . Taking these numbers into equation (4) allows us to calculate the binding  $K_d$  via Eq. 5:

$$K_d = [C_0 \times (1 - \text{QE})]^2 / (C_0 \times \text{QE}) = C_0 \times (1 - \text{QE})^2 / \text{QE} \quad (\text{Eq. 5})$$

To measure QE more accurately, a plot of  $(\text{QE} \times C)$  vs.  $C$  ( $C =$  lectin concentration) over a lectin concentration range below Gx-DiMan surface saturation was employed to determine the average QE from linear fitting, where the slope obtained from the fit represents the average QE (see SI, Figs. S12E & S18). The fitting parameters and calculated  $K_d$ s using Eq. 5 for DC-SIGN/R binding with Gx-DiMan at various glycan densities were summarised in **Table 1**.

Table 1. Summary of the average QEs and apparent  $K_{ds}$  for Gx-DiMan (x = 5, 13, and 27) binding with DC-SIGN/R (after correction of the QE background obtained from the Gx-OH control).

Gx-DiMan	DC-SIGN		DC-SIGNR	
	QE	$K_d$ (nM)	QE	$K_d$ (nM)
G5-DiMan100%	0.473 ± 0.012	5.8 nM	0.314 ± 0.006	14.9 nM
G13-DiMan100%	0.603 ± 0.003	1.0 nM	0.445 ± 0.001	2.7 nM
G13-DiMan75%	0.535 ± 0.004	1.6 nM	0.397 ± 0.008	3.6 nM
G13-DiMan50%	0.462 ± 0.008	2.5 nM	0.349 ± 0.006	4.8 nM
G13-DiMan25%	0.391 ± 0.014	3.8 nM	0.348 ± 0.004	4.9 nM
G27-DiMan100%	0.523 ± 0.025	0.2 nM	0.367 ± 0.006	0.54 nM
G27-DiMan75%	0.468 ± 0.017	0.3 nM	0.313 ± 0.011	0.75 nM
G27-DiMan50%	0.490 ± 0.016	0.26 nM	0.314 ± 0.011	0.75 nM
G27-DiMan25%	0.400 ± 0.025	0.45 nM	0.296 ± 0.017	0.83 nM

Based on the calculated  $K_{ds}$  (Table 1), four notable conclusions can be drawn: (1) DC-SIGN bound more strongly to all Gx-DiMans than DC-SIGNR did, irrespective of the GNP size and glycan density. As G5-DiMan here presents a good mimic for the HIV's trimeric gp120 spike, its stronger affinity with DC-SIGN over DC-SIGNR thus may help explain why DC-SIGN is more effective than DC-SIGNR in transmitting HIV infections.<sup>36</sup> This result agreed well with our earlier results obtained with QD-DiMan<sup>19</sup> and G5-DiMan conjugates.<sup>11</sup> Given that the CRDs in DC-SIGN/R have the same mannose-binding motifs,<sup>34</sup> the different affinities here may indicate that the DC-SIGN/R might adopt different modes in binding to Gx-DiMan, similar to those observed previously with QD-DiMan<sup>19</sup> and G5-DiMan.<sup>11</sup> (2) The MLGI affinity between Gx-DiMan and DC-SIGN/R increased significantly with the increasing GNP scaffold size. For example, the  $K_{ds}$  for Gx-DiMan (x = 5, 13, and 27 nm) were found to be ~5.8, ~1.0, and ~0.2 nM for DC-SIGN, and ~14.9, ~2.7, and ~0.54 nM for DC-SIGNR, respectively, suggesting that a larger GNP scaffold provided a more favourable glycan display to enhance DC-SIGN/R binding. This is likely due to the lower surface curvature of larger GNP scaffolds which improves their surface glycan access to DC-SIGN/R CRDs for multivalent binding.<sup>29</sup> (3) Decreasing the Gx surface glycan density gradually weakened their MLGI affinities for both lectins. This result was also consistent with the literature that glycoconjugates of larger sizes and higher glycan valency generally offered higher viral inhibition potencies.<sup>4-5, 58</sup> (4) G27-DiMan (100%) exhibited the strongest DC-SIGN affinity among all Gx-DiMan conjugates studied here, with an apparent  $K_d$  of ~0.2 nM, its affinity was ~29 and ~5 folds stronger than its G5- and G13- DiMan(100%) counterparts. Interestingly, the same trend was also observed for DC-SIGNR binding with Gx-DiMan. This result indicates that increasing GNP scaffold size is strongly beneficial for enhancing their MLGI affinities

with DC-SIGN/R, likely due to the reduced surface curvature in G27 which affords the glycan ligands a more suitable spatial topology for forming strong MLGIs with both lectins.<sup>29</sup>

### Probing DC-SIGN/R-Gx-DiMan Binding Mode by Dynamic Light Scattering

G13-DiMan (100%) and G27-DiMan (100%) were employed to investigate their binding modes with unlabeled wild-type (WT)-DC-SIGN/R (no cysteine mutation) by dynamic light scattering (DLS).<sup>11, 29</sup> First, we monitored the  $D_h$ s of binding induced Gx-DiMan-lectin assemblies under a variety of protein: GNP molar ratios (PGRs) using a fixed concentration of 5 nM for G13-DiMan or 1 nM for G27-DiMan. Both WT-DC-SIGN and DC-SIGNR alone displayed a single  $D_h$  species of ~12 nm with a narrow size distribution with a full width at half-maximum, FWHM, of ~3.7 nm from Gaussian fitting (see SI, Fig. S10). The resulting  $D_h$  histograms (volume population) of Gx-DiMan-DC-SIGN/R complexes under a variety of PGRs were shown in SI, Figs. S22-25. Their  $D_h$  – PGR relationships were shown in Fig. 3A. In general, the average  $D_h$  of the Gx-DiMan-DC-SIGN complexes increased gradually with the increasing PGR before reaching saturation, where the  $D_h$  remained roughly constant. However, the trend of  $D_h$  - PGR relationship for DC-SIGN was found to be significantly different from that of DC-SIGNR; the latter consistently yielded larger  $D_h$ s than the former. The saturated  $D_h$ s for DC-SIGN binding with G13-DiMan and G27-DiMan were found to be ~60 and ~75 nm, respectively, which roughly match those expected for a single Gx-DiMan particle coated with a single layer of DC-SIGN molecules.<sup>31, 34</sup> In contrast, the  $D_h$ s of the Gx-DiMan-DC-SIGNR complexes (*e.g.*, ~200 and ~500 nm for  $x = 13$  and  $27$ , respectively) were found to be too big to be isolated single particles, and thus indicating the formation of aggregation or cluster induced by DC-SIGNR and G13/G27-DiMan crosslinking. This result is comparable to that observed with G5-DiMan previously.<sup>11</sup> Using a surface binding footprint of ~35 nm<sup>2</sup> per DC-SIGN molecule,<sup>19</sup> and the glycan surface areas of Gx-DiMan calculated from their  $D_h$ s, a PGR of ~42 or ~92 with DC-SIGN was estimated to be able to fully saturate the surface of G13-DiMan or G27-DiMan, respectively.

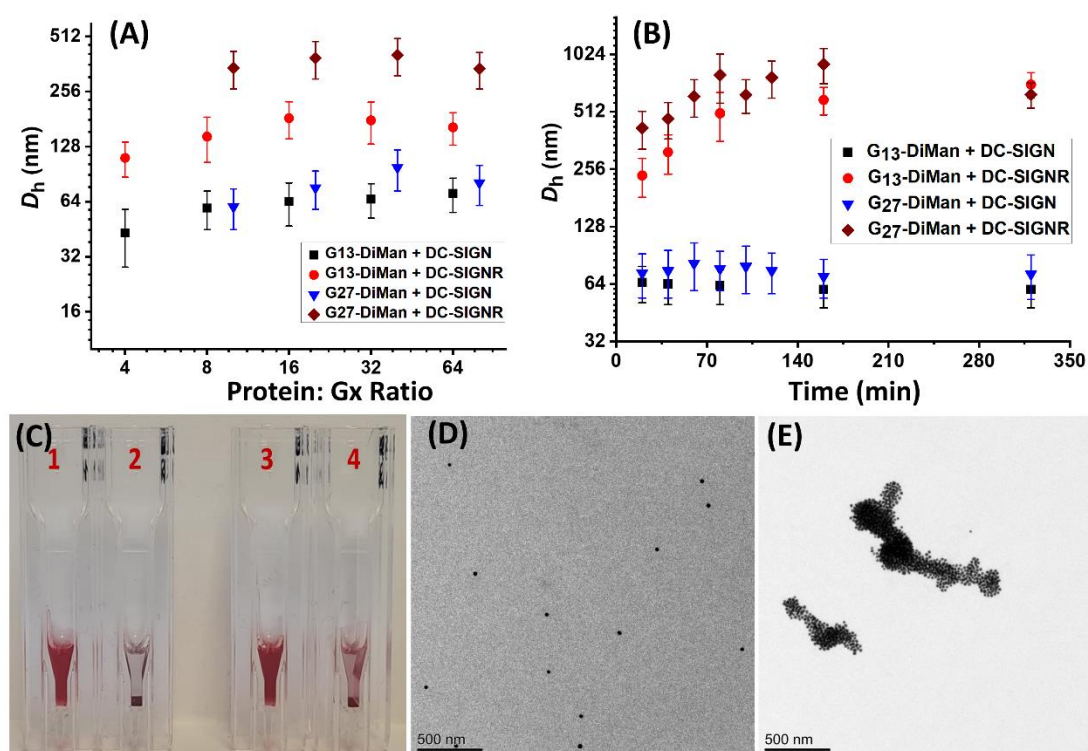


Figure 2. (A) hydrodynamic diameter ( $D_h$ , volume population) - PGR relationship for G13/27-DiMan binding with DC-SIGN/R, and (B)  $D_h$ -Time relationship for G13/27-DiMan binding with DC-SIGN/R under a fixed PGR of 32 or 80 for G13-DiMan or G27-DiMan, respectively.  $D_h$  values (volume population) are displayed as Mean  $D_h \pm \frac{1}{2}$  FWHM. For distributions containing two different  $D_h$  species, mean  $D_h = (x_{c1}.A_1\%) + (x_{c2}.A_2\%)$ ; and mean FWHM =  $(w_1.A_1\%) + (w_2.A_2\%)$ . (C) Optical photographs of representative DLS samples at 5 h after mixing Gx-DiMan and lectins: (1) G27-DiMan + DC-SIGN (PGR: 80); (2) G27-DiMan + DC-SIGNR (PGR: 80); (3) G13-DiMan + DC-SIGN (PGR: 32); (4) G13-DiMan + DC-SIGNR (PGR: 32). (D, E) TEM images of cryo-prepared G27-DiMan + DC-SIGN (D) or G27-DiMan + DC-SIGNR (E) samples after 40 min incubation (PGR = 80) in a binding buffer. Scale bar = 500 nm.

The  $D_h$  - time evolution of binding-induced Gx-DiMan-DC-SIGN/R complexes was also monitored by DLS and shown in Fig. 2B. The corresponding time-dependent  $D_h$  distribution (volume population) histograms were given in SI, Figs. S26-S29. The binding of DC-SIGN with G13/27-DiMan gave only a single gaussian species with a  $D_h$  of  $\sim 60$  nm and  $\sim 77$  nm, respectively. Such species formed very rapidly ( $< 20$  min) and showed no further changes in  $D_h$  over the next 320 mins. These results are consistent with DC-SIGN binding simultaneously to one Gx-DiMan *via* all four of its CRDs, thereby forming a single layer of DC-SIGN molecules on each Gx-DiMan particle to give isolated single Gx-

DiMan particles.<sup>11, 19</sup> In contrast, binding of DC-SIGNR gave considerably larger  $D_h$ s at 20 mins (e.g., >200 and > 400 nm for G13-/G27-DiMan, respectively), which also showed significant increases with time (e.g., >600 and 900 nm for G13-/G27-DiMan at 160 min) and finally stayed at ~700 nm at 320 min. Such  $D_h$  values were far too large to be individual Gx-DiMan coated with a monolayer of proteins, a strong indication of DC-SIGNR and G13/G27-DiMan crosslinking to form large GNP-lectin assemblies. Such crosslinking reactions happened over a relatively long period, leading to gradually increased assemblies over time and eventually precipitated out of the solution after 5 h (Fig. 2C). In contrast, DC-SIGN-Gx-DiMan assemblies were highly stable and showed no signs of precipitation after 5 h (Fig. 2C). Overall, these results indicated that the mode of G13/27-DiMan binding with DC-SIGN and DC-SIGNR were clearly different: DC-SIGN binds simultaneously with all four CRDs to a single Gx-DiMan and forms small, isolated single particles, whereas DC-SIGNR and Gx-DiMan crosslink each other to form large scale assemblies.

The different binding modes of Gx-DiMan with DC-SIGN/R were further verified by “cryo-snapshot” TEM imaging, which has been shown to be able to capture nanoparticle in their native dispersion states in solution.<sup>59</sup> This was achieved by rapid plunge-freezing of the sample into liquid ethane, followed by drying under vacuum and finally loading on the TEM grids for TEM imaging.<sup>11, 59</sup> Here, G27-DiMan was employed in the investigation. G27-DiMan was first mixed with DC-SIGN or DC-SIGNR at a PGR of 80 and incubated for 40 mins, then they were plunge-frozen for sample preparation and finally applied for TEM imaging. The resulting TEM images (Figs. 2D, E) clearly revealed that binding of DC-SIGN with G27-DiMan gave completely isolated single particles, whereas binding of DC-SIGNR produced large-scale clustered GNPs. These results fully agreed with their  $D_h$  sizes described in the previous section. The combined TEM and DLS data thus reaffirmed the distinct modes for DC-SIGN/R in binding to G27-DiMan, where DC-SIGN binds simultaneously with all four binding sites to one G27-DiMan to form small, isolated GNP/protein core/shell particles, while DC-SIGNR crosslinks with different G27-DiMan particles to form large scale GNP-protein assemblies. These results completely agree with those observed previously between DC-SIGN/R and G5-DiMan or (4 nm) QD-DiMan.<sup>11, 19</sup> Therefore, increasing the Gx-DiMan scaffold size from 5 to 27 nm did not alter their binding mode with DC-SIGN/R in the solution, although it did significantly enhance their MLGI affinities.

### **Probing Gx-DiMan Binding Thermodynamics with DC-SIGN/R**

The binding thermodynamics between Gx-DiMan and DC-SIGN/R were derived by measuring their apparent  $K_{dS}$  *via* GNP fluorescence quenching at three different temperatures (e.g., 25, 30, and 35 °C).

The temperature was controlled by a dry bath for samples, and the cuvette temperature was maintained by using a temperature-controlled water pump system.<sup>28</sup> The resulting fluorescence spectra and the (QE x C) versus C plots were given in SI, Figs. S30-S34. The apparent  $K_d$ s and fitting parameters were summarized in SI, Table S4. The calculated  $K_d$ s at different temperatures were then combined with Van't Hoff analysis to derive the binding thermodynamic data. By integrating the two Gibbs free energy equations (Eqs. 6 and 7), the resulting changes in the MLGI enthalpy ( $\Delta H$ ) and entropy ( $\Delta S$ ) terms can be obtained from the linear fits of the  $\ln(K_d)$  vs.  $(1/T)$  plots using Eq. 8.<sup>28</sup>

$$\Delta G = -RT\ln(K_a) = RT\ln(K_d) \quad (\text{Eq. 6})$$

$$\Delta G = \Delta H - T\Delta S \quad (\text{Eq. 7})$$

$$\ln K_d = \frac{\Delta H}{R} \left( \frac{1}{T} \right) - \frac{\Delta S}{R} \quad (\text{Eq. 8})$$

Where  $\Delta G$  is the change of the binding Gibbs free energy,  $K_a$  is the equilibrium association constant,  $K_d$  is the equilibrium dissociation constant (where  $K_a = 1/K_d$ ),  $T$  is the absolute temperature in degrees Kelvin, and  $R$  is the ideal gas constant.

Figs. 3A and 3B showed the Van't Hoff plots and linear fits of the Gx-DiMan - DC-SIGN/R binding data. The slope and intercept obtained from the linear fits correspond to the  $(\Delta H/R)$  and  $(-\Delta S/R)$ , respectively. The resulting MLGI thermodynamic parameters for Gx-DiMan binding DC-SIGN/R were shown schematically in Fig. 3C, and the detailed thermodynamic parameters were summarized in Table 2.

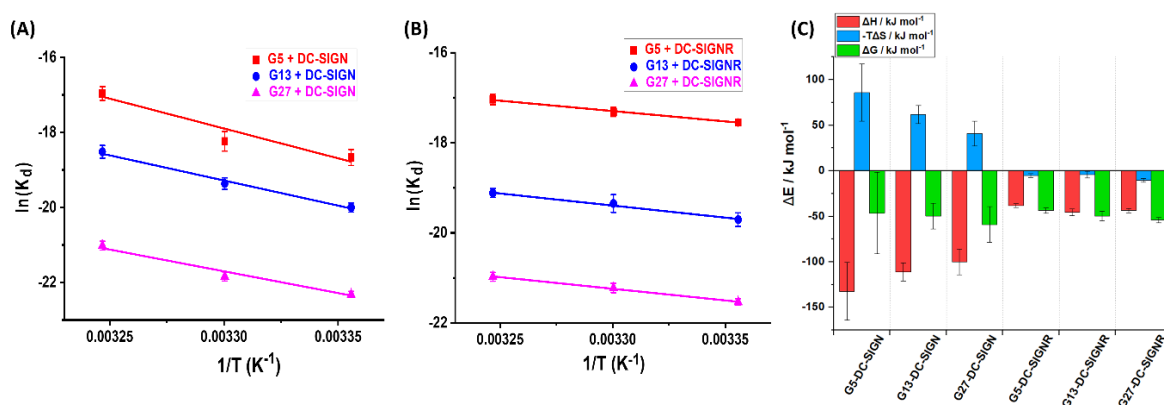


Figure 3. Van't Hoff analyses of the  $\ln(K_d) - 1/T$  relationships for Gx-DiMan binding with (A) DC-SIGN and (B) DC-SIGNR. All data have been corrected for Gx's inner filter effects obtained with their respective Gx-OH negative control. (C) Comparison of the standard ( $T = 298$  K) binding  $\Delta H$  (red),  $T.\Delta S$  (blue), and  $\Delta G$  (green) for Gx-DiMan binding with DC-SIGN/R. Error bars represent the fitting errors.

Table 2. Summary of the MLGI thermodynamic parameters for Gx-DiMan binding with DC-SIGN/R under standard conditions (T = 298K). Error bars represent the fitting errors.

<b>Gx-DiMan – Lectin</b>	<b><math>\Delta H^0</math> (kJ mol<sup>-1</sup>)</b>	<b><math>\Delta S^0</math> (J mol<sup>-1</sup> K<sup>-1</sup>)</b>	<b><math>-T\Delta S^0</math> (kJ mol<sup>-1</sup>)</b>	<b><math>\Delta G^0</math> (kJ mol<sup>-1</sup>)</b>
<b>G5-DiMan - DC-SIGN</b>	-132 ± 32	-288 ± 105	86 ± 31	-47 ± 44
<b>G13-DiMan – DC-SIGN</b>	-111 ± 10	-207 ± 33	62 ± 9	-50 ± 14
<b>G27-DiMan – DC-SIGN</b>	-100 ± 14	-138 ± 46	41 ± 14	-59 ± 19
<b>G5- DiMan – DC-SIGNR</b>	-38.2 ± 2.0	17.6 ± 6.0	-5.2 ± 2.0	-43.5 ± 3.0
<b>G13-DiMan – DC-SIGNR</b>	-45.5 ± 4.0	14.3 ± 11.0	-4.2 ± 4.0	-49.7 ± 5.0
<b>G27-DiMan – DC-SIGNR</b>	-43.8 ± 2.0	34.9 ± 7.0	-10.4 ± 2.0	-54.2 ± 3.0

Two notable conclusions can be drawn from the results shown in Table 2. (1) DC-SIGN binding interactions with all three Gx-DiMan (x = 5, 13 and 27) are enthalpy-driven with strong negative  $\Delta H$  terms. Their binding  $\Delta H^0$  values were found to be similar (after accounting for the experimental errors) at  $-132 \pm 32$ ,  $-111 \pm 10$  and  $-100 \pm 14$  kJ mol<sup>-1</sup>, for x = 5, 13, and 27, respectively. These  $\Delta H^0$  values are roughly 4 times that of the monovalent DC-SIGN CRD-DiMan measured with ITC ( $-25.8$  kJ mol<sup>-1</sup>),<sup>60</sup> suggesting that all four CRDs in each DC-SIGN have participated in binding to Gx-DiMan. This result further supports our conclusion of the tetravalent binding mode for DC-SIGN described in the previous section. The good agreement of  $\Delta H^0$  values obtained here with those measured in ITC suggests that our GNP fluorescence quenching can act as a reliable new method for probing DC-SIGN MLGI thermodynamics. (2) The  $\Delta S^0$  values for Gx-DiMan-DC-SIGN binding were found to reduce gradually with the increasing GNP scaffold size. The total MLGI entropy changes reflect the net contributions of the binding induced changes in translational, rotational, and conformational entropies of lectins and Gx-DiMan ligands as well as their surrounding media (*e.g.* binding buffer).<sup>28</sup> Therefore, a likely reason for the reduced entropic penalty for the bigger GNPs observed here could be due to the presence of more free, unbound DiMan ligands on their surfaces (measurements performed at PGRs below surface saturation) which are flexible (anchored to the GNP surface *via* hydrophilic, flexible EG<sub>4</sub> linkers), and thus they have largely retained their conformational and rotational degrees of freedom. Taking together, the thermodynamic data of DC-SIGN-Gx-DiMan binding obtained here are consistent to that expected for DC-SIGN based on its simultaneous tetravalent binding mode described in the earlier sections.

In contrast, the binding thermodynamics of DC-SIGNR were found to differ significantly from those of DC-SIGN. The highly favourable  $\Delta H^0$  values obtained in DC-SIGN were significantly reduced for DC-SIGNR binding with all three Gx-DiMans. The  $\Delta H^0$ s of DC-SIGNR binding with all three Gx-DiMans were similar, and at  $\sim$ half those obtained with DC-SIGN. This result may indicate that only the binding/or unbinding of two CRDs in DC-SIGNR-Gx-DiMan interactions were captured under our experimental conditions. This result is consistent with the  $D_h$  studies where DC-SIGNR cross-links with different Gx-DiMans, presumably first using 2 CRDs to form partially bound Gx-DiMan-DC-SIGNR structural units, which then crosslink each other to form large assemblies.<sup>28</sup> The later step may happen over a relatively long period and hence may not be captured in the current measurement. Interestingly, the large entropic penalties observed in DC-SIGN binding appeared to have diminished and replaced with a small favourable entropic term. Overall, these results indicate that DC-SIGNR binding exhibits a smaller favourable enthalpy term than that observed for DC-SIGN, although this has been partially compensated by a small favourable entropic term,<sup>61</sup> leading to only slightly smaller binding  $\Delta G^0$ s than those of DC-SIGN.

#### **Inhibition of DC-SIGN/R-promoted EBOV<sub>pp</sub> entry into cells.**

Given the strong affinities (low apparent  $K_{ds}$ ) of Gx-DiMan in binding to DC-SIGN/R, we anticipated that they should be strong inhibitors in blocking DC-SIGN/R-mediated viral infections, exemplified using the pseudo-Ebola virus. Therefore, Gx-DiMans were tested for their ability to inhibit cell surface DC-SIGN/R promoted entry of the pseudo-Ebola virus using a model cellular infection assay.<sup>11, 19</sup> Here, single cycle murine leukaemia virus (MLV) particles pseudotyped with the Ebola virus glycoprotein (EBOV-GP) and encoding the luciferase gene were used (EBOV<sub>pp</sub>).<sup>11, 19</sup> As target cells, we employed human embryonic kidney cells, 293T, transfected to express DC-SIGN and DC-SIGNR, as described previously.<sup>11, 19</sup> This well-established cellular assay provides a robust readout (luciferase activity indicating infectious entry) for evaluating antiviral properties of glycoconjugates targeting DC-SIGN/R.<sup>11, 19</sup> Binding of Gx-DiMan to cell surface DC-SIGN/R will block these lectin receptors from binding to EBOV-GP spikes on the virus surface, reducing virus cellular entry and hence luciferase production as shown in SI, Fig. S35 schematically. MLV particles bearing the vesicular stomatitis virus glycoprotein (VSV-G) that does not employ DC-SIGN/R for cell entry were employed as specificity control, while MLV particles encoding luciferase but bearing no viral glycoprotein were used as negative control.<sup>11</sup> All experiments assessing antiviral activity of Gx-DiMan (positive controls) and Gx-OH (negative controls) were performed in DMEM cell culture medium supplemented with 10% fetal bovine serum (FBS) at 37 °C as described previously.<sup>11</sup> The unprocessed luciferase activities of 293T cells treated with Gx-DiMan and Gx-OH controls were given in SI, Figs. S36-S37. After Gx-

DiMan treatment, luciferase activity upon EBOV<sub>pp</sub> infection were significantly and dose-dependently reduced, while those measured upon VSV-G-driven infections were almost unaffected. Moreover, treatment with the Gx-OH control lacking the terminal DiMan showed no apparent inhibition (SI, Fig. S37). These results clearly indicated that the observed inhibitions were specific, due to specific binding of Gx-DiMan to cell surface DC-SIGN/R receptors, precluding subsequent binding to EBOV-GP and augmentation of infection. The normalized viral inhibition data were fitted by a modified inhibition model described in Eq. 9:<sup>11, 43</sup>

$$NA = \frac{1}{\left[1 + \left(\frac{C}{EC_{50}}\right)^n\right]} \quad (\text{Eq. 9})$$

Where  $NA$ ,  $EC_{50}$ ,  $C$ , and  $n$  are the normalized luciferase activity, Gx-DiMan concentration giving 50% apparent inhibition, Gx-DiMan concentration, and inhibition coefficient, respectively. Here, the  $n$  value indicates how quickly an inhibitor can achieve complete inhibition by increasing concentration, with  $n < 1$ ,  $= 1$ , or  $> 1$  indicating an inhibition being negatively-, non- or positively- cooperative, respectively.<sup>43</sup> In general, any viable viral inhibitors should have  $n \geq 1$  (with  $n = 1$  being the most widely observed), so that they can achieve completely inhibit virus infection under a reasonable concentration.<sup>43</sup> The normalised luciferase activities (infections) for samples after each treatment were plotted against the dose of Gx-DiMan and fitted by Eq. 9 and the results were shown in Fig. 4. The detailed fitting parameters were summarized in Table 3.

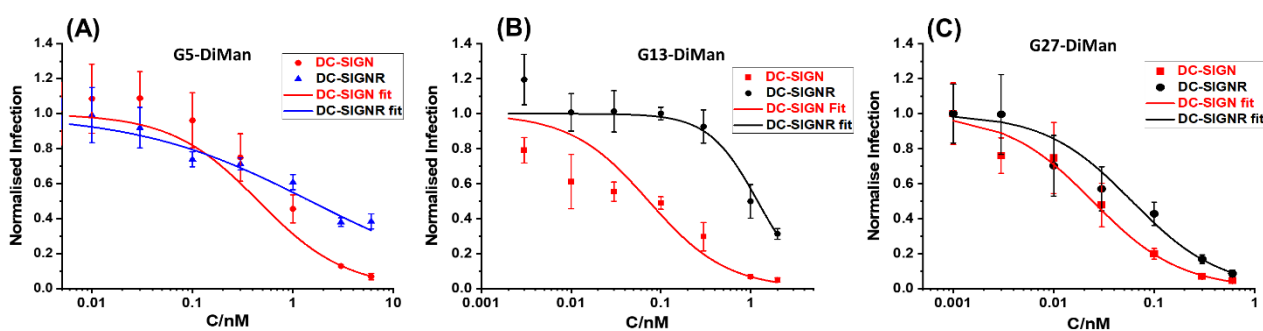


**Figure 4.** Plots of normalised luciferase activity (NA) as a function of Gx-DiMan concentration for the 293T cells after treatment with varying doses of Gx-DiMan and the data were fitted by Eq. 9. The luciferase activities for all treatment samples were subtracted by their corresponding pcDNA control backgrounds and then normalized by corresponding values obtained in the absence of Gx-DiMan.

It was exciting that all three Gx-DiMan (x = 5, 13, and 27) conjugates potently and non-cooperatively blocked DC-SIGN promoted EBOV<sub>pp</sub> entry into 293T cells, with impressively low  $EC_{50}$  values of  $0.45 \pm 0.002$ ,  $0.073 \pm 0.007$ , and  $0.023 \pm 0.001$  nM, respectively. Thus, their antiviral potency was found to be enhanced with the increasing GNP scaffold size. This was fully consistent with their enhanced DC-SIGN affinity measured by the GNP fluorescence quenching assay (Table 1). Moreover, all three Gx-DiMan inhibitors were found to act in a non-cooperative fashion ( $n = 1$ ), indicating that Gx-DiMan could serve as viable, potent inhibitor of DC-SIGN mediated viral infections. Notably, G27-DiMan, with an impressively low  $EC_{50}$  of  $23 \pm 1$  pM, is considerably more potent than some of the most potent glycoconjugate inhibitors reported in literature (e.g., the giant globular multivalent glycofullerenes,  $EC_{50}$ :  $\sim 0.67$  nM,<sup>15</sup> the virus-like glycodendrinanoparticles,  $EC_{50}$ :  $\sim 0.91$  nM,<sup>18</sup> and our previous QD-EG<sub>3</sub>-DiMan,  $EC_{50}$ :  $\sim 0.70$  nM,<sup>19</sup> and G5-EG<sub>2</sub>-DiMan,  $EC_{50}$ :  $\sim 0.095$  nM<sup>11</sup>). Interestingly, compared to G5-EG<sub>2</sub>-DiMan (G5 coated by an identical LA-EG<sub>m</sub>-DiMan ligand except for the linker being two EG unit shorter), G5-DiMan here was found to be potent ( $EC_{50}$ :  $\sim 0.45$  nM vs.  $\sim 0.095$  nM<sup>11</sup>), consistent to its weaker DC-SIGN binding affinity ( $K_d$ :  $\sim 5.8$  nM vs.  $\sim 3.8$  nM<sup>11</sup>). Thus, increasing the EG<sub>m</sub> linker length weakened the DC-SIGN binding affinity and antiviral potency of GNP-glycans, similar to that observed previously with QD-DiMan conjugates.<sup>19</sup> Nonetheless, a suitable EG linker length is required for glycan-nanoparticles to promote high stability and resisting non-specific interactions,<sup>41</sup> which are essential for potential applications under the challenging in vivo conditions.

**Table 3:** Summary of inhibition data obtained for Gx-DiMan (x = 5, 13 and 27) against cell surface DC-SIGN/R receptors mediated pseudo-Ebola virus infection of 293T cells.

Gx-DiMan	Lectin receptor	n	EC <sub>50</sub> (nM)	R <sup>2</sup>
G5-DiMan	DC-SIGN	1	$0.45 \pm 0.02$	0.959
G13-DiMan	DC-SIGN	1	$0.073 \pm 0.007$	0.948
G27-DiMan	DC-SIGN	1	$0.023 \pm 0.001$	0.980
G5-DiMan	DC-SIGNR	$0.50 \pm 0.06$	$1.49 \pm 0.23$	0.942
G13-DiMan	DC-SIGNR	$1.59 \pm 0.25$	$1.19 \pm 0.10$	0.987
G27-DiMan	DC-SIGNR	1	$0.049 \pm 0.002$	0.976

The inhibition of DC-SIGNR-promoted EBOV<sub>pp</sub> entry by Gx-DiMan was also enhanced with the increasing GNP scaffold size (i.e., with  $EC_{50}$  values of  $1.5 \pm 0.2$ ,  $1.2 \pm 0.1$ , and  $0.049 \pm 0.002$  nM for G5-, G13-, and G27- DiMan, respectively), similar to that observed against DC-SIGN mediated infections. However, their inhibition cooperativity showed a clear scaffold size dependence: it changed

from negative ( $n = \sim 0.5$ ) to positive ( $n = \sim 1.6$ ) and finally non-cooperative ( $n = 1$ ) as GNP scaffold size increased from 5 to 27 nm. This may indicate a change of binding behaviour (or mode) for Gx-DiMan with cell surface DC-SIGNR receptors as scaffold size changes. While the smallest G5-DiMan may retain its crosslinking mode in binding to DC-SIGNR on the cell surface which makes it difficult to achieve complete inhibition ( $n < 1$ ) due to cell membrane restrictions, the largest G27-DiMan may be able to bind simultaneously to a single DC-SIGNR receptor and completely block its binding to EBOV-GP, similar to that occurring with DC-SIGN on cell membrane, giving rise to non-cooperative inhibition ( $n = 1$ ). Together with an impressively low  $EC_{50}$  of  $\sim 49$  pM, these results indicate that G27-DiMan can serve as a potent, viable inhibitor against DC-SIGNR mediated viral infection. Given that both DC-SIGN and DC-SIGNR have shown to play an important role in facilitating SARS-CoV-2 infections,<sup>33</sup> the excellent potency and non-cooperative inhibition behaviour observed with G27-DiMan may make it a highly promising, viable entry inhibitor against SARS-CoV-2 infections.

Interestingly, a  $\sim 2.2$ -fold higher potency for G27-DiMan against DC-SIGN- over DC-SIGNR-mediated viral infections also agreed well with their relative MLGI affinity differences measured by fluorescence quenching (*i.e.*,  $K_d$ :  $\sim 0.20$  vs.  $\sim 0.54$  nM). A comparison of the MLGI affinities measured by fluorescence quenching with viral inhibition data revealed that the  $K_d$  and  $EC_{50}$  values do not match directly, possibly due to the different binding environments used in these studies (*e.g.*, solution vs. cell membrane).<sup>11</sup> However, there appeared to have a clear positive correlation between the  $K_d$  and  $EC_{50}$  values (*i.e.*, the lower the  $K_d$ , the lower the  $EC_{50}$ , signifying more potent inhibition). This result suggests that our GNP quenching method developed here could act as a rapid method for estimating relative antiviral potentials for GNP-glycan based entry inhibitors.

## Conclusion

In summary, we have developed a new GNP fluorescence quenching assay format which has successfully addressed the potential interference arising from GNP's strong inner filter effect, making it suitable for measuring the MLGI affinities and thermodynamics for both small and large GNP-glycans. Using this assay, we have revealed that both DC-SIGN/R MLGI affinities are strongly dependent and enhanced significantly (by  $\sim 30$  fold) as the GNP scaffold size increases from 5 to 27 nm. DC-SIGN binding with Gx-DiMan is enthalpy driven, with strong negative MLGI  $\Delta H$  values of  $\sim 4$  times that of the corresponding monovalent binding, suggesting all four of its CRDs are engaged in binding. This matches well with its simultaneous tetravalent binding mode observed from the hydrodynamic size and TEM analyses of binding-induced lectin-GNP assemblies. Finally, we have

demonstrated that Gx-DiMans are potent entry inhibitors against DC-SIGN/R mediated pseudo-Ebola virus cellular infection, and their antiviral potencies are enhanced significantly with the increasing GNP size. In particular, G27-DiMan potently and robustly ( $n = 1$ ) blocks both DC-SIGN and DC-SIGNR mediated virus infection with impressively low  $EC_{50}$ s of  $\sim 23$  and  $\sim 49$  pM, respectively, making it the most potent glycoconjugate inhibitor against DC-SIGN/R- mediated Ebola cellular infections. Our work thus demonstrates the great potential of G27-DiMan as a highly potent entry inhibitor against a wide range of DC-SIGN/R-promoted viral infections.

## Experimental Section

**Materials.** Gold (III) chloride trihydrate, sodium hydroxide, trisodium citrate, copper sulphate, sodium sulphate, calcium chloride, HEPES, lipoic acid (LA), sodium ascorbate, Tris[(1-benzyl-1H-1,2,3-triazol-4-yl)methyl] amine (TBTA), methanol, ethanol, chloroform, phenol, bovine serum albumin, tetrahydrofuran, tris-(hydroxymethyl)aminomethane (Tris base), hydrochloric acid, sodium chloride, ethylenediamine tetraacetic acid (EDTA), guanidine hydrochloride were purchased from Sigma-Aldrich, Alfa Aesar, Fluorochem, and Thermo Scientific with >99% purity and used as-received without further purification unless specified elsewhere. 2-[2-(2-Azido-ethoxy) ethoxy]ethanol and 5 nm citrate-stabilized GNPs were purchased from Sigma-Aldrich.  $\text{NH}_2\text{-EG}_4\text{-C}\equiv\text{CH}$  was purchased PurePEG LLC. Maleimide modified Atto-643 dye was commercially purchased from ATTO-Tech GmbH. Ultrapure water (resistance >18.2 M $\Omega$ .cm) purified by an ELGA Purelab classic UVF system was used for all experiments and making all buffers.

**Synthesis of 13 nm Gold Nanoparticles (G13s).**<sup>45, 62</sup> Freshly prepared aqueous solution of gold (III) chloride trihydrate (1 mM, 400 mL) was placed in a 500 mL three-necked round-bottomed flask, and the solution was then heated to reflux in an oil bath (130 °C) under stirring. When the solution began to reflux, trisodium citrate solution (38 mM, 40 mL) was quickly added. The solution colour quickly turned from yellow to wine red in  $\sim 1$  min, indicating the formation of GNPs. The reaction was further refluxed under magnetic stirring for another 1 hr to ensure the reaction was complete. The GNP solution was then removed from the oil bath and was allowed to cool down to room temperature (RT) naturally under stirring. This produced citrate-stabilized GNPs with a core diameter of  $\sim 13$  nm as confirmed by TEM imaging (SI, Fig. S1). The resulting G13 stock was transferred to a clean glass container and stored at RT till use.

**Synthesis of 27 nm Gold Nanoparticles (G27s).**<sup>45, 62</sup> Freshly prepared aqueous solution of gold (III) chloride trihydrate (0.25 mM, 400 mL) was placed in a 500 mL two-necked round-bottomed flask, and NaOH (1 mM, 50 mL) was then added directly into the solution. The mixture was stirred for 30 mins and then heated to reflux in a 130 °C oil bath under magnetic stirring. After the solution started to reflux, trisodium citrate solution (166 mM, 6 mL) was then quickly added. The solution colour gradually changed from yellow to light red in 15 mins. The reaction was refluxed for another 1 hr to complete the synthesis. The solution was then taken out of the oil bath and kept stirring for 1 hr till it was cooled down to RT. This produced citrate stabilized GNPs with a mean diameter of ~27 nm (G27) as confirmed by TEM images (see SI, Fig. S2). The G27 stock was transferred to a clean glass container and stored at RT till use.

**Synthesis of LA-EG<sub>4</sub>-DiMan.**<sup>11</sup> LA-EG<sub>4</sub>-C≡CH was synthesized amide coupling between lipoic acid (LA) and commercial NH<sub>2</sub>-EG<sub>4</sub>-C≡CH as described previously.<sup>43</sup> 1-Azido-3,6-dioxaoct-8-yl- $\alpha$ -D-mannopyranosyl-(1 $\rightarrow$ 2)- $\alpha$ -D-manno-pyranoside (N<sub>3</sub>-EG<sub>2</sub>-DiMan) was synthesized *via* our established protocols as described previously.<sup>19</sup> LA-EG<sub>4</sub>-C≡CH (50 mg, 0.120 mmol), N<sub>3</sub>-EG<sub>2</sub>-DiMan (66 mg, 0.132 mmol), CuSO<sub>4</sub>·5H<sub>2</sub>O (1.07 mg, 0.0043 mmol), TBTA (4.01 mg, 0.0075 mmol), and sodium ascorbate (3.21 mg, 0.0162 mmol) were dissolved in 2 mL of THF/H<sub>2</sub>O (1:1, vol/vol) to allow for efficient click reaction between LA-EG<sub>4</sub>-C≡CH and N<sub>3</sub>-EG<sub>2</sub>-DiMan.<sup>11</sup> The resulting solution was stirred overnight at RT in darkness. The next day, the consumption of all starting compounds was confirmed by TLC. The solvent was then evaporated, and the desired ligand was purified by size exclusion chromatography using Biogel P2 column using ammonium formate as an eluent to afford the desired product, LA-EG<sub>4</sub>-DiMan, in 77% yield.<sup>11</sup> TLC: (CHCl<sub>3</sub>/MeOH 3:1) R<sub>f</sub> 0.57; <sup>1</sup>H NMR (400 MHz, D<sub>2</sub>O)  $\delta$  (ppm): 8.10 (s, 1H), 5.12 (s, 1H), 5.03 (s, 1H), 4.73 – 4.60 (m, 3H), 4.08 (s, 1H), 3.99 (dd, 3H, *J*=10.2, 5.1 Hz), 3.94 – 3.82 (m, 5H), 3.69 (dt, 31H, *J*=12.8, 7.1, 6.7 Hz), 3.45 – 3.30 (m, 2H), 3.30 – 2.33 (m, 2H), 2.26 (t, 2H, *J*=7.3 Hz), 1.99 (dt, 1H, *J*=12.9, 6.9 Hz), 1.78 – 1.54 (m, 4H), 1.42 (q, 1H, *J*=7.6 Hz); <sup>13</sup>C NMR (100 MHz, D<sub>2</sub>O)  $\delta$  (ppm): 176.7, 144.1, 125.5, 102.2, 98.3, 78.6, 73.2, 72.7, 70.2, 70.1, 69.9, 69.6, 69.6, 69.5, 69.5, 69.4, 69.2, 68.9, 68.8, 68.7, 66.9, 66.8, 66.5, 66.5, 63.2, 63.1, 61.4, 61.1, 60.8, 59.3, 56.5, 50.1, 50.0, 46.6, 40.2, 38.9, 38.1; LC-MS: calculated *m/z* for C<sub>37</sub>H<sub>66</sub>N<sub>4</sub>O<sub>18</sub>S<sub>2</sub> (M+H)<sup>+</sup> 919.38, found 919.78 (see SI, Fig. S3).

**Synthesis of LA-EG<sub>4</sub>-OH.**<sup>11</sup> LA-EG<sub>4</sub>-C≡CH (50 mg, 0.120 mmol), 2-[2-(2-Azido-ethoxy) ethoxy] ethanol, N<sub>3</sub>-EG<sub>2</sub>-OH (23.1 mg, 0.132 mmol), CuSO<sub>4</sub>·5H<sub>2</sub>O (1.07 mg, 0.0043 mmol), TBTA (4.01 mg, 0.0075 mmol), and sodium ascorbate (3.21 mg, 0.0162 mmol) were dissolved in 2 mL of THF/H<sub>2</sub>O (1:1, vol/vol) to allow for efficient click reaction between LA-EG<sub>4</sub>-C≡CH and N<sub>3</sub>-EG<sub>2</sub>-OH. The resulting solution was stirred overnight at RT in darkness. The next day, the consumption of all starting

compounds was confirmed by TLC. The solvent was then evaporated, and the desired ligand was purified by size exclusion chromatography using Biogel P2 column using ammonium formate as an eluent to obtain the desired product in 75% yield.<sup>11</sup> TLC: (CHCl<sub>3</sub>/MeOH 10:1) R<sub>f</sub> 0.45; <sup>1</sup>H NMR (500 MHz, D<sub>2</sub>O) δ (ppm): 8.01 (s, 1H), 3.93 – 3.87 (m, 2H), 3.66 – 3.59 (m, 17H), 3.58 – 3.56 (m, 4H), 3.55 – 3.51 (m, 5H), 3.48 – 3.45 (m, 2H), 3.29 (t, 2H, *J*=5.2 Hz), 3.15 – 3.07 (m, 1H), 2.39 (dq, 1H, *J*=12.4, 6.1 Hz), 2.16 (t, 2H, *J*=7.3 Hz), 1.88 (dq, 1H, *J*=13.8, 6.9 Hz), 1.70 – 1.60 (m, 1H), 1.53 (ddd, 3H, *J*=14.9, 7.6, 5.3 Hz), 1.31 (p, 2H, *J*=7.6 Hz); <sup>13</sup>C NMR (125 MHz, D<sub>2</sub>O) δ (ppm): 183.1, 142.9, 125.4, 71.6, 69.6, 69.4, 68.9, 68.7, 65.9, 61.5, 60.3, 56.4, 49.9, 48.4, 43.9, 43.7, 43.2, 41.7, 38.0, 36.3, 33.6, 33.4, 24.9, 17.3; LC-MS: calculated *m/z* for C<sub>25</sub>H<sub>46</sub>N<sub>4</sub>O<sub>8</sub>S<sub>2</sub> (M+H)<sup>+</sup> 595.28, found 595.57 (see SI, Fig. S4).

**Preparation of Gx-DiMan/OH Conjugates.** G5-DiMans were prepared by mixing G5 and LA-EG<sub>4</sub>-DiMan ligand *via* self-assembly in an aqueous solution.<sup>11</sup> Commercially G5s (6 mL, 91 nM) suspended in citrate solution were concentrated to 250 μL using a 30 K MWCO spin column and washed with H<sub>2</sub>O (3 × 250 μL) to remove any unbound impurities. The resulting concentrated G5 solution was then directly mixed with LA-EG<sub>4</sub>-DiMan ligand at a G5: ligand molar ratio of 1: 1 000. The resulting mixture was left stirring at RT in darkness overnight to form G5-DiMan conjugates. After that, the mixture was transferred to a 30 K MWCO centrifugal filter and centrifuged at 4 000 rpm for 20 mins, and the G5-DiMan residues was washed with H<sub>2</sub>O (3 × 250 μL) to remove any unbound free ligands, and then dispersed in pure water to make the G5-DiMan stock. Its concentration was determined by the Beer–Lambert law from the plasmon peak absorbance at ~515 nm and molar extinction coefficient of 1.10 × 10<sup>7</sup> M<sup>-1</sup>cm<sup>-1</sup> for G5 (see SI, Fig. S5 for *D<sub>h</sub>* histogram and UV-vis spectrum).

For the preparation of G13/27-DiMan, 20 mL each of the citrate stabilized G13 or G27 stock solution was directly added with the required amount of LA-EG<sub>4</sub>-DiMan ligand stock solution in water at a GNP: ligand molar ratio of 1:3 000 for G13 or 1:10 000 for G27. The resulting solution was stirred at RT in the dark overnight to make the Gx-DiMan conjugates *via* gold-thiol self-assembly. After that, the resulting mixtures were divided into 1.5 mL portions into eppendorf tubes and centrifuged at 17 000 × *g* for 30 mins for G13-DiMan or 6 000 × *g* for 15 mins for G27-DiMan conjugates to remove any unbound free ligands. After careful withdrawal of supernatant, the Gx-DiMan residues were washed with pure water (3 × 500 μL), followed by centrifugation three times to remove any unbound free ligands. For G27, the eppendorf tubes were pre-washed with 0.025% Tween-20 aqueous solution before being used in Gx-DiMan purification to prevent nanoparticle sticking to the eppendorf walls.

To prepare Gx-DiMan conjugates with different surface glycan densities (e.g., 75%, 50% and 25%), LA-EG<sub>4</sub>-OH and LA-EG<sub>4</sub>-DiMan were mixed in the desired percentages first before being used in GNP conjugation under the same total ligand: Gx molar ratios and purified using the same method as Gx-DiMan. The  $D_h$  histograms and UV-vis spectra for G13/27-DiMan/-OH were given in Fig. S6 and S7 (SI). The concentrations of Gx-DiMan/OH conjugates were determined by the Beer–Lambert law using their peak absorbance at ~520 nm and molar extinction coefficient of  $2.32 \times 10^8 \text{ M}^{-1}\text{cm}^{-1}$  for G13, and  $2.39 \times 10^9 \text{ M}^{-1}\text{cm}^{-1}$  for G27, respectively (see SI, Fig. S8).

All the filtrate and washing-through liquids were collected, combined, freeze-dried, and re-dissolved in 1.40 mL pure water to determine the amount of unbound LA-EG<sub>4</sub>-DiMan ligand using the phenol-sulphuric acid method described previously.<sup>11, 19</sup> 25  $\mu\text{L}$  of each solution was diluted with water to a final volume of 125  $\mu\text{L}$ . This solution was then mixed with 125  $\mu\text{L}$  of 5% phenol and 625  $\mu\text{L}$  of  $\text{H}_2\text{SO}_4$ , and then allowed to incubate at RT for 30 mins. The absorbance of the solution was recorded at 490 nm, and the dilution factors were then corrected to calculate the total amount of unconjugated glycan ligand against a standard calibration curve obtained with pure LA-EG<sub>4</sub>-DiMan ligand. The difference in LA-EG<sub>4</sub>-DiMan ligand amount between that added and that remained in the supernatant was conserved to have conjugated onto the GNP surface.<sup>11</sup>

**Protein Production and Labeling.**<sup>11, 19</sup> The soluble extracellular segments of DC-SIGN and DC-SIGNR, which faithfully replicated the tetrameric structure and glycan binding properties of full length lectins,<sup>11, 19</sup> were expressed as inclusion bodies in *E. coli* and purified by mannose-Sepharose affinity column followed by Superdex size exclusion column as reported previously.<sup>27</sup> The mutant proteins, DC-SIGN Q-274C and DC-SIGNR R278C, were constructed by site-directed mutagenesis and labeled with Atto-643 maleimide as described previously.<sup>19, 28</sup> The labeled proteins were purified by mannose-Sepharose affinity columns. All the proteins were characterized by high-resolution mass spectroscopy (HRMS, see SI, Figs. S9 and S11). The dye labeling efficiency (per protein monomer) was determined to be ~82% and ~90% for DC-SIGN and DC-SIGNR, respectively, based on the relative peak areas of the labeled and unlabeled protein peaks measured by HR-MS (see SI, Fig. S11).

**Fluorescence Spectra.**<sup>11</sup> All fluorescence spectra were recorded on a Horiba FluoroMax-4 Spectrofluorometer using a 0.70 mL quartz cuvette under a fixed excitation wavelength ( $\lambda_{\text{ex}}$ ) of 630 nm. Emission spectra over 650-800 nm were collected with excitation and emission slit widths of 5 nm under a slow scan speed. All measurements were carried out in a binding buffer (20 mM HEPES, pH 7.8, 100 mM NaCl, 10 mM  $\text{CaCl}_2$ ) containing 1 mg/mL BSA to reduce any non-specific interactions and absorption to cuvette walls. The required amounts of Gx-DiMan and DC-SIGN/R were mixed and

then incubated at RT for 20 mins before recording their fluorescence spectra. The fluorescence spectra from 650 to 800 nm were integrated and used to calculate the quenching efficiency (QE).

**Dynamic Light Scattering (DLS).**<sup>11</sup> All DLS measurements were performed on a Malvern Zetasizer NanoZS DLS system using a sample volume of 400  $\mu$ L in 1 cm disposable polystyrene cuvettes. The hydrodynamic diameters ( $D_h$ , all volume populations) of wild-type DC-SIGN/R, Gx-DiMan and Gx-DiMan + DC-SIGN or DC-SIGNR samples were measured in a binding buffer (20 mM HEPES, 100 mM NaCl, 10 mM CaCl<sub>2</sub>, pH 7.8) at RT with ten consecutive runs, and each lasting 120 seconds, and the averages of the ten runs were used to determine size distributions. Each sample was analyzed in triplicate to obtain their average  $D_h$  and standard deviations (SDs).

**Data Analysis and Fitting.**<sup>11</sup> All fluorescence and DLS data were analyzed using the Origin software (version 2022b). The fluorescence spectra of lectins alone and lectin + Gx-DiMan samples were integrated and used to calculate the QEs and presented as mean  $\pm$  standard errors (SEs). The (QE  $\times$  C) vs. C plots were fitted by linear function, accounting for the SEs of each data point, to give the best fits (highest  $R^2$  values). The DLS histograms were fitted by the standard Gaussian function (single or multiple, depending on the data) to obtain the  $D_h$  (shown as Xc in the fitting parameters), full-width at half-maximum (FWHM, shown as W), and area abundance (shown as A) and depicted in each DLS graph. For samples containing two species, a linear average of the two based on their volume abundances were used, e.g., mean  $D_h = D_{h1} \times A_1/(A_1+A_2) + D_{h2} \times A_2/(A_1+A_2)$ ; mean FWHM =  $FWHM_1 \times A_1/(A_1+A_2) + FWHM_2 \times A_2/(A_1+A_2)$ .<sup>11</sup> The results obtained from the best fits were listed in the relevant tables with the standard fitting errors.

## ASSOCIATED CONTENT

**Supporting Information.** Materials, instruments, and methods showing the synthesis and characterization of LA-EG<sub>4</sub>-DiMan and LA-EG<sub>4</sub>-OH ligands by <sup>1</sup>H/<sup>13</sup>C NMR and MS spectra, the production, characterization and labeling of DC-SIGN/R; UV-vis, DLS histograms and TEM images of citrate stabilized G13 and G27; DLS histograms of Gx-DiMan and Gx-DiMan-lectin complexes under different protein to GNP ratios and their time dependent evolution; the fluorescence spectra of lectins alone and lectin + Gx-DiMan samples under different molar ratios and under three different temperatures, and the resulting (QE  $\times$  C) vs. C plots with linear fits; and the unprocessed virus inhibition data. “This material is available free of charge via the Internet at <http://pubs.acs.org>.”

## AUTHOR INFORMATION

### Corresponding Author

**Yuan Guo**- *School of Food Science and Nutrition, and Astbury Centre for Structural Molecular Biology, University of Leeds, Leeds LS2 9JT, United Kingdom.*

Orcid.org/0000-0003-4607-7356

Email: [y.guo@leeds.ac.uk](mailto:y.guo@leeds.ac.uk).

**Dejian Zhou**- *School of Chemistry, and Astbury Centre for Structural Molecular Biology, University of Leeds, Leeds LS2 9JT, United Kingdom.*

Orcid.org/0000-0003-3314-9242

Email: [d.zhou@leeds.ac.uk](mailto:d.zhou@leeds.ac.uk)

### Author

**Rahman Basaran** - *School of Food Science and Nutrition, and Astbury Centre for Structural Molecular Biology, University of Leeds, Leeds LS2 9JT, United Kingdom.*

**Darshita Budhadev**- *School of Chemistry and Astbury Centre for Structural Molecular Biology, University of Leeds, Leeds LS2 9JT, United Kingdom.*

**Amy Kempf** – Infection Biology Unit, German Primate Center, Leibniz Institute for Primate Research, 37077 Göttingen, Germany.

**Inga Nehlmeier** – Infection Biology Unit, German Primate Center, Leibniz Institute for Primate Research, 37077 Göttingen, Germany.

**Nicole Hondow**- *School of Chemical and Process Engineering, University of Leeds, Leeds LS2 9JT, United Kingdom.*

**Stefan Pöhlmann** – Infection Biology Unit, German Primate Center-Leibniz Institute for Primate Research, and Faculty of Biology and Psychology, University of Göttingen, Göttingen 37073, Germany.

### Conflict of Interests

**There is no conflicting Interest to declare.**

### Data Availability

The data that support the findings of this study are available from the corresponding author upon request. For the purpose of open access, the authors have applied a Creative Commons Attribution (CC BY) license to any Author Accepted Manuscript version arising from this submission.

### Funding Sources

This project was supported by a UK Biotechnology and Biological Science Research Council grant (grant number: BB/R007829/1, to D.Z., N.H., & Y.G.)

### Acknowledgement

This project was supported by a UK Biotechnology and Biological Science Research Council grant (grant number: BB/R007829/1). R.B. thanks the Turkish Ministry of National Education for providing a PhD scholarship to support his study at the University of Leeds, United Kingdom.

## References

1. Brown, G. D.; Willment, J. A.; Whitehead, L., C-type lectins in immunity and homeostasis. *Nat. Rev. Immunol.* **2018**, *18* (6), 374-389.
2. Geijtenbeek, T. B. H.; Gringhuis, S. I., Signalling through C-type lectin receptors: shaping immune responses. *Nat. Rev. Immunol.* **2009**, *9* (7), 465-479.
3. Mammen, M.; Choi, S. K.; Whitesides, G. M., Polyvalent interactions in biological systems: implications for design and use of multivalent ligands and inhibitors. *Angew. Chem. Int. Ed.* **1998**, *37* (20), 2754-2794.
4. Bernardi, A.; Jiménez-Barbero, J.; Casnati, A.; De Castro, C.; Darbre, T.; Fieschi, F.; Finne, J.; Funken, H.; Jaeger, K. E.; Lahmann, M.; Lindhorst, T. K.; Marradi, M.; Messner, P.; Molinaro, A.; Murphy, P. V.; Nativi, C.; Oscarson, S.; Penadés, S.; Peri, F.; Pieters, R. J.; Renaudet, O.; Reymond, J. L.; Richichi, B.; Rojo, J.; Sansone, F.; Schäffer, C.; Turnbull, W. B.; Velasco-Torrijos, T.; Vidal, S.; Vincent, S.; Wennekes, T.; Zuilhof, H.; Imberty, A., Multivalent glycoconjugates as anti-pathogenic agents. *Chem. Soc. Rev.* **2013**, *42* (11), 4709-4727.
5. Bhatia, S.; Camacho, L. C.; Haag, R., Pathogen Inhibition by Multivalent Ligand Architectures. *J. Am. Chem. Soc.* **2016**, *138* (28), 8654-66.
6. Branson, T. R.; McAllister, T. E.; Garcia-Hartjes, J.; Fascione, M. A.; Ross, J. F.; Warriner, S. L.; Wennekes, T.; Zuilhof, H.; Turnbull, W. B., A Protein-Based Pentavalent Inhibitor of the Cholera Toxin B-Subunit. *Angew. Chem. Int. Ed.* **2014**, *53* (32), 8323-8327.
7. Kitov, P. I.; Sadowska, J. M.; Mulvey, G.; Armstrong, G. D.; Ling, H.; Pannu, N. S.; Read, R. J.; Bundle, D. R., Shiga-like toxins are neutralized by tailored multivalent carbohydrate ligands. *Nature* **2000**, *403* (6770), 669-672.
8. Huskens, J.; Prins, L. J.; Haag, R.; Ravoo, B. J., *Multivalency: concepts, research and applications*. John Wiley & Sons: 2018.
9. Feinberg, H.; Castelli, R.; Drickamer, K.; Seeberger, P. H.; Weis, W. I., Multiple modes of binding enhance the affinity of DC-SIGN for high mannose N-linked glycans found on viral glycoproteins. *J. Biol. Chem.* **2007**, *282* (6), 4202-4209.
10. Illescas, B. M.; Rojo, J.; Delgado, R.; Martin, N., Multivalent Glycosylated Nanostructures To Inhibit Ebola Virus Infection. *J. Am. Chem. Soc.* **2017**, *139* (17), 6018-6025.
11. Budhadev, D.; Poole, E.; Nehlmeier, I.; Liu, Y.; Hooper, J.; Kalverda, E.; Akshath, U. S.; Hondow, N.; Turnbull, W. B.; Pöhlmann, S., Glycan-gold nanoparticles as multifunctional probes for multivalent lectin-carbohydrate binding: implications for blocking virus infection and nanoparticle assembly. *J. Am. Chem. Soc.* **2020**, *142* (42), 18022-18034.
12. Chen, X.; Ramström, O.; Yan, M., Glyconanomaterials: Emerging applications in biomedical research. *Nano Res.* **2014**, *7* (10), 1381-1403.
13. Lasala, F.; Arce, E.; Otero, J. R.; Rojo, J.; Delgado, R., Mannosyl glycodendritic structure inhibits DC-SIGN-mediated Ebola virus infection in *cis* and in *trans*. *Antimicrob. Agents Chemoth.* **2003**, *47* (12), 3970-3972.
14. Martínez-Ávila, O.; Hijazi, K.; Marradi, M.; Clavel, C.; Campion, C.; Kelly, C.; Penadés, S., Gold Manno-Glyconanoparticles: Multivalent Systems to Block HIV-1 gp120 Binding to the Lectin DC-SIGN. *Chem. Eur. J.* **2009**, *15* (38), 9874-9888.
15. Muñoz, A.; Sigwalt, D.; Illescas, B. M.; Luczkowiak, J.; Rodríguez-Pérez, L.; Nierengarten, I.; Holler, M.; Remy, J. S.; Buffet, K.; Vincent, S. P.; Rojo, J.; Delgado, R.; Nierengarten, J. F.; Martín, N., Synthesis of giant globular multivalent glycofullerenes as potent inhibitors in a model of Ebola virus infection. *Nat. Chem.* **2016**, *8* (1), 50-7.

16. Ramos-Soriano, J.; Reina, J. J.; Illescas, B. M.; De La Cruz, N.; Rodriguez-Perez, L.; Lasala, F.; Rojo, J.; Delgado, R.; Martín, N., Synthesis of highly efficient multivalent disaccharide/[60] fullerene nanoballs for emergent viruses. *J. Am. Chem. Soc.* **2019**, *141* (38), 15403-15412.
17. Reichardt, N. C.; Martín-Lomas, M.; Penadés, S., Glyconanotechnology. *Chem. Soc. Rev.* **2013**, *42* (10), 4358-4376.
18. Ribeiro-Viana, R.; Sánchez-Navarro, M.; Luczkowiak, J.; Koeppe, J. R.; Delgado, R.; Rojo, J.; Davis, B. G., Virus-like glycodendrinanoparticles displaying quasi-equivalent nested polyvalency upon glycoprotein platforms potently block viral infection. *Nat. Commun.* **2012**, *3* (1), 1303.
19. Guo, Y.; Nehlmeier, I.; Poole, E.; Sakonsiri, C.; Hondow, N.; Brown, A.; Li, Q.; Li, S.; Whitworth, J.; Li, Z.; Yu, A.; Brydson, R.; Turnbull, W. B.; Pöhlmann, S.; Zhou, D., Dissecting Multivalent Lectin–Carbohydrate Recognition Using Polyvalent Multifunctional Glycan-Quantum Dots. *J. Am. Chem. Soc.* **2017**, *139* (34), 11833-11844.
20. Illescas, B. M.; Rojo, J.; Delgado, R.; Martín, N., Multivalent glycosylated nanostructures to inhibit Ebola virus infection. *J. Am. Chem. Soc.* **2017**, *139* (17), 6018-6025.
21. Porkolab, V.; Lepsík, M.; Ordanini, S.; St John, A.; Le Roy, A.; Thépaut, M.; Paci, E.; Ebel, C.; Bernardi, A.; Fieschi, F., Powerful Avidity with a Limited Valency for Virus-Attachment Blockers on DC-SIGN: Combining Chelation and Statistical Rebinding with Structural Plasticity of the Receptor. *ACS Cent. Sci.* **2023**, *9* (4), 709-718.
22. Porkolab, V.; Pifferi, C.; Sutkeviciute, I.; Ordanini, S.; Taouai, M.; Thépaut, M.; Vivès, C.; Benazza, M.; Bernardi, A.; Renaudet, O.; Fieschi, F., Development of C-type lectin-oriented surfaces for high avidity glycoconjugates: towards mimicking multivalent interactions on the cell surface. *Org. Biomol. Chem.* **2020**, *18* (25), 4763-4772.
23. Velazquez-Campoy, A.; Freire, E., Isothermal titration calorimetry to determine association constants for high-affinity ligands. *Nat. Protoc.* **2006**, *1* (1), 186-191.
24. Wang, X.; Ramström, O.; Yan, M. D., Glyconanomaterials: Synthesis, Characterization, and Ligand Presentation. *Adv. Mater.* **2010**, *22* (17), 1946-1953.
25. Liyanage, S. H.; Yan, M. D., Quantification of binding affinity of glyconanomaterials with lectins. *Chem. Commun.* **2020**, *56* (88), 13491-13505.
26. Rao, J. H.; Lahiri, J.; Isaacs, L.; Weis, R. M.; Whitesides, G. M., A trivalent system from vancomycin•D-Ala-D-Ala with higher affinity than avidin•biotin. *Science* **1998**, *280* (5364), 708-711.
27. Guo, Y.; Sakonsiri, C.; Nehlmeier, I.; Fascione, M. A.; Zhang, H.; Wang, W.; Pöhlmann, S.; Turnbull, W. B.; Zhou, D., Compact, polyvalent mannose quantum dots as sensitive, ratiometric FRET probes for multivalent protein–ligand interactions. *Angew. Chem. Int. Ed.* **2016**, *55* (15), 4738-4742.
28. Hooper, J.; Liu, Y. Y.; Budhadev, D.; Ainaga, D. F.; Hondow, N.; Zhou, D. J.; Guo, Y., Polyvalent Glycan Quantum Dots as a Multifunctional Tool for Revealing Thermodynamic, Kinetic, and Structural Details of Multivalent Lectin-Glycan Interactions. *ACS Appl. Mater. Interfaces* **2022**, *14* (42), 47385-47396.
29. Hooper, J.; Budhadev, D.; Ainaga, D. L. F.; Hondow, N.; Zhou, D. J.; Guo, Y., Polyvalent Glycan Functionalized Quantum Nanorods as Mechanistic Probes for Shape-Selective Multivalent Lectin-Glycan Recognition. *ACS Appl. Nano Mater.* **2023**, *6* (6), 4201-4213.
30. Geijtenbeek, T. B. H.; Kwon, D. S.; Torensma, R.; van Vliet, S. J.; van Duijnhoven, G. C. F.; Middel, J.; Cornelissen, I.; Nottet, H.; KewalRamani, V. N.; Littman, D. R.; Figdor, C. G.; van Kooyk, Y., DC-SIGN, a dendritic cell-specific HIV-1-binding protein that enhances *trans*-infection of T cells. *Cell* **2000**, *100* (5), 587-597.
31. Guo, Y.; Feinberg, H.; Conroy, E.; Mitchell, D. A.; Alvarez, R.; Blixt, O.; Taylor, M. E.; Weis, W. I.; Drickamer, K., Structural basis for distinct ligand-binding and targeting properties of the receptors DC-SIGN and DC-SIGNR. *Nat. Struct. Mol. Biol.* **2004**, *11* (7), 591-598.
32. Pöhlmann, S.; Soilleux, E. J.; Baribaud, F.; Leslie, G. J.; Morris, L. S.; Trowsdale, J.; Lee, B.; Coleman, N.; Doms, R. W., DC-SIGNR, a DC-SIGN homologue expressed in endothelial cells, binds to human and simian immunodeficiency viruses and activates infection in trans. *Proc. Natl. Acad. Sci. U. S. A.* **2001**, *98* (5), 2670-2675.

33. Amraei, R.; Yin, W.; Napoleon, M. A.; Suder, E. L.; Berrigan, J.; Zhao, Q.; Olejnik, J.; Chandler, K. B.; Xia, C.; Feldman, J., CD209L/L-SIGN and CD209/DC-SIGN act as receptors for SARS-CoV-2. *ACS Cent. Sci.* **2021**, *7* (7), 1156-1165.
34. Feinberg, H.; Mitchell, D. A.; Drickamer, K.; Weis, W. I., Structural basis for selective recognition of oligosaccharides by DC-SIGN and DC-SIGNR. *Science* **2001**, *294* (5549), 2163-6.
35. Guo, Y.; Atkinson, C. E.; Taylor, M. E.; Drickamer, K., All but the shortest polymorphic forms of the viral receptor DC-SIGNR assemble into stable homo- and heterotetramers. *J. Biol. Chem.* **2006**, *281* (24), 16794-16798.
36. Chung, N. P. Y.; Breun, S. K. J.; Bashirova, A.; Baumann, J. G.; Martin, T. D.; Karamchandani, J. M.; Rausch, J. W.; Le Grice, S. F. J.; Wu, L.; Carrington, M.; KewalRamani, V. N., HIV-1 Transmission by Dendritic Cell-specific ICAM-3-grabbing Nonintegrin (DC-SIGN) Is Regulated by Determinants in the Carbohydrate Recognition Domain That Are Absent in Liver/Lymph Node-SIGN (L-SIGN). *J. Biol. Chem.* **2010**, *285* (3), 2100-2112.
37. Davis, C. W.; Nguyen, H. Y.; Hanna, S. L.; Sánchez, M. D.; Doms, R. W.; Pierson, T. C., West Nile virus discriminates between DC-SIGN and DC-SIGNR for cellular attachment and infection. *J. Virol.* **2006**, *80* (3), 1290-1301.
38. Susumu, K.; Uyeda, H. T.; Medintz, I. L.; Pons, T.; Delehanty, J. B.; Mattoussi, H., Enhancing the Stability and Biological Functionalities of Quantum Dots via Compact Multifunctional Ligands. *J. Am. Chem. Soc.* **2007**, *129* (45), 13987-13996.
39. Zhou, D. J.; Bruckbauer, A.; Abell, C.; Klenerman, D.; Kang, D. J., Fabrication of three-dimensional surface structures with highly fluorescent quantum dots by surface-templated layer-by-layer assembly. *Adv. Mater.* **2005**, *17* (10), 1243-1248.
40. Prime, K. L.; Whitesides, G. M., Self-Assembled Organic Monolayers - Model Systems for Studying Adsorption of Proteins at Surfaces. *Science* **1991**, *252* (5009), 1164-1167.
41. Prime, K. L.; Whitesides, G. M., Adsorption of Proteins onto Surfaces Containing End-Attached Oligo(ethylene oxide) - A Model System Using Self-Assembled Monolayers. *J. Am. Chem. Soc.* **1993**, *115* (23), 10714-10721.
42. Zhou, D.; Bruckbauer, A.; Ying, L. M.; Abell, C.; Klenerman, D., Building three-dimensional surface biological assemblies on the nanometer scale. *Nano Lett.* **2003**, *3* (11), 1517-1520.
43. Budhadev, D.; Hooper, J.; Rocha, C.; Nehlmeier, I.; Kempf, A. M.; Hoffmann, M.; Krüger, N.; Zhou, D. J.; Pöhlmann, S.; Guo, Y., Polyvalent Nano-Lectin Potently Neutralizes SARS-CoV-2 by Targeting Glycans on the Viral Spike Protein. *JACS Au* **2023**, *3*, 1755-1766.
44. Ji, X.; Song, X.; Li, J.; Bai, Y.; Yang, W.; Peng, X., Size Control of Gold Nanocrystals in Citrate Reduction: The Third Role of Citrate. *J. Am. Chem. Soc.* **2007**, *129* (45), 13939-13948.
45. Song, L.; Ho, V. H. B.; Chen, C.; Yang, Z. Q.; Liu, D. S.; Chen, R. J.; Zhou, D. J., Efficient, pH-Triggered Drug Delivery Using a pH-Responsive DNA-Conjugated Gold Nanoparticle. *Adv. Healthc. Mater.* **2013**, *2* (2), 275-280.
46. Stewart-Jones, G. B. E.; Soto, C.; Lemmin, T.; Chuang, G.-Y.; Druz, A.; Kong, R.; Thomas, P. V.; Wagh, K.; Zhou, T.; Behrens, A.-J.; Bylund, T.; Choi, C. W.; Davison, J. R.; Georgiev, I. S.; Joyce, M. G.; Kwon, Y. D.; Pancera, M.; Taft, J.; Yang, Y.; Zhang, B.; Shivatare, S. S.; Shivatare, V. S.; Lee, C.-C. D.; Wu, C.-Y.; Bewley, C. A.; Burton, D. R.; Koff, W. C.; Connors, M.; Crispin, M.; Baxa, U.; Korber, B. T.; Wong, C.-H.; Mascola, J. R.; Kwong, P. D., Trimeric HIV-1-Env Structures Define Glycan Shields from Clades A, B, and G. *Cell* **2016**, *165* (4), 813-826.
47. Lee, J. H.; Ozorowski, G.; Ward, A. B., Cryo-EM structure of a native, fully glycosylated, cleaved HIV-1 envelope trimer. *Science* **2016**, *351* (6277), 1043-8.
48. Saha, S. K.; Brewer, C. F., Determination of the concentrations of oligosaccharides, complex type carbohydrates, and glycoproteins using the phenol-sulfuric acid method. *Carbohydr. Res.* **1994**, *254*, 157-67.
49. Hill, H. D.; Millstone, J. E.; Banholzer, M. J.; Mirkin, C. A., The role radius of curvature plays in thiolated oligonucleotide loading on gold nanoparticles. *ACS Nano* **2009**, *3* (2), 418-24.
50. Dubertret, B.; Calame, M.; Libchaber, A. J., Single-mismatch detection using gold-quenched fluorescent oligonucleotides. *Nat. Biotech.* **2001**, *19* (4), 365-370.

51. Jennings, T. L.; Singh, M. P.; Strouse, G. F., Fluorescent Lifetime Quenching near  $d = 1.5$  nm Gold Nanoparticles: Probing NSET Validity. *J. Am. Chem. Soc.* **2006**, *128* (16), 5462-5467.
52. Dulkeith, E.; Ringler, M.; Klar, T. A.; Feldmann, J.; Muñoz Javier, A.; Parak, W. J., Gold nanoparticles quench fluorescence by phase induced radiative rate suppression. *Nano Lett* **2005**, *5* (4), 585-9.
53. Pons, T.; Medintz, I. L.; Sapsford, K. E.; Higashiya, S.; Grimes, A. F.; English, D. S.; Mattoussi, H., On the quenching of semiconductor quantum dot photoluminescence by proximal gold nanoparticles. *Nano Lett.* **2007**, *7* (10), 3157-3164.
54. Seferos, D. S.; Giljohann, D. A.; Hill, H. D.; Prigodich, A. E.; Mirkin, C. A., Nano-flares: Probes for transfection and mRNA detection in living cells. *J. Am. Chem. Soc.* **2007**, *129* (50), 15477-15479.
55. Song, S. P.; Liang, Z. Q.; Zhang, J.; Wang, L. H.; Li, G. X.; Fan, C. H., Gold-Nanoparticle-Based Multicolor Nanobeacons for Sequence-Specific DNA Analysis. *Angew. Chem. Int. Ed.* **2009**, *48* (46), 8670-8674.
56. Liu, X.; Atwater, M.; Wang, J.; Huo, Q., Extinction coefficient of gold nanoparticles with different sizes and different capping ligands. *Coll. Surf. B.* **2007**, *58* (1), 3-7.
57. Zhang, H. Y.; Feng, G. Q.; Guo, Y.; Zhou, D. J., Robust and specific ratiometric biosensing using a copper-free clicked quantum dot-DNA aptamer sensor. *Nanoscale* **2013**, *5* (21), 10307-10315.
58. Boisselier, E.; Astruc, D., Gold nanoparticles in nanomedicine: preparations, imaging, diagnostics, therapies and toxicity. *Chem. Soc. Rev.* **2009**, *38* (6), 1759-1782.
59. Hondow, N.; Brydson, R.; Wang, P. Y.; Holton, M. D.; Brown, M. R.; Rees, P.; Summers, H. D.; Brown, A., Quantitative characterization of nanoparticle agglomeration within biological media. *J. Nanopart. Res.* **2012**, *14* (7), 977.
60. Holla, A.; Skerra, A., Comparative analysis reveals selective recognition of glycans by the dendritic cell receptors DC-SIGN and Langerin. *Prot. Eng. Des. Select.* **2011**, *24* (9), 659-669.
61. Chodera, J. D.; Mobley, D. L., Entropy-Enthalpy Compensation: Role and Ramifications in Biomolecular Ligand Recognition and Design. In *Annual Rev. Biophys.*, Dill, K. A., Ed. 2013; Vol. 42, pp 121-142.
62. Song, L.; Guo, Y.; Roebuck, D.; Chen, C.; Yang, M.; Yang, Z. Q.; Sreedharan, S.; Glover, C.; Thomas, J. A.; Liu, D. S.; Guo, S. R.; Chen, R. J.; Zhout, D. J., Terminal PEGylated DNA-Gold Nanoparticle Conjugates Offering High Resistance to Nuclease Degradation and Efficient Intracellular Delivery of DNA Binding Agents. *ACS Appl. Mater. Interfaces* **2015**, *7* (33), 18707-18716.